Search for Black Holes and String Balls in ATLAS

Master Degree Thesis in Experimental Particle Physics

by

Jørn Havås Mæland

Department of Physics and Technology
University of Bergen
Norway

June 2010

Acknowledgements

I would like to thank my supervisor Gerald Eigen for all the help I have received during this period. Secondly I would like to thank Maren Ugland for all her help in making my root ntuples for this study and answering my questions. Thirdly I would like to thank Thomas Burgess for helping me with my programing problems. And lastly, I would like to thank my fellow students and staff within the particle physic group at the University of Bergen, and Helene for helping me with correcting spelling errors.

June 1, 2010

Jørn Havås Mæland

ii

Preface

Theories that include extra dimension, may change the Planck scale to the order of the electroweak symmetry breaking scale. This may allow for the creation of black hole and string balls at particle physics experiments, like those at the Large Hadron Collider. The decay of black holes and sting balls will have unique signatures, that allows us to discover them. The main focus for this thesis have been to studying the decay of simulated black holes and string balls. Where we have been focusing on methods to remove standard model backgrounds from our signal selection. If black hole and string balls are able to be produced at the Large Hadron Collider, we conclude that ATLAS will have great discovery potential for black holes and string balls.

In Chapter 1 a very short introduction to black holes are given, while in Chapter 2 a short description of the Standard Model of particle physics is given. In Chapter 3, we introduce the concept of extra dimensions and explain black hole and string balls in more details.

In Chapter 4 and 5 we give a short description of LHC and explain the ATLAS detector in more detail. We introduce the data formats and analysis framework that are used within the ATLAS experiment. The concept of Monte Carlo generated data is also introduced here.

Results from our black hole analysis is presented in chapter 6, and the string balls results are presented in chapter 7. Finally, a summary is given in chapter 8.

Contents

List of Tables

List of Figures

Chapter 1

Introduction

When one thinks about black holes, the first that often comes to mind is astronomical black holes, these galactic objects with its enormous gravitational force. While these objects seem far away, and our possibility of studying them is only through astrophysical observation, it may be that mini black holes can be produced in particle collision. Thus, at particle physics experiments, like those at the Large Hadron Collider, we may be able to create and observe mini black holes. If these mini black holes exist and are observed at LHC, black holes can teach us much about our universe. For instance, they may give us evidence for existence of extra dimensions as well as a better understanding of the fundamental forces of nature. Figure 1.1 shows a simulated black hole that decays inside the ATLAS detector. The decay of such a black hole is expected to be one of the more spectacular events in particle physics, because it decays into many particles and will deposit a huge amount of energy in a particle detector.
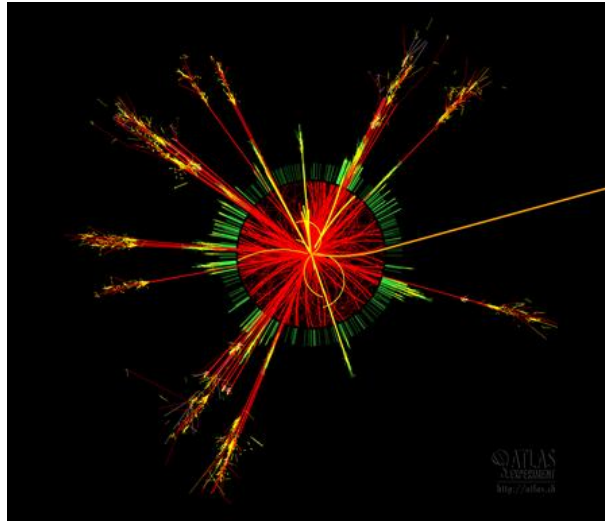
Figure 1.1: Simulated black hole decaying in the ATLAS detector [1].

Chapter 2

Standard Model

There are four fundamental forces of nature, the strong, the electromagnetic, the weak and the gravitational force. The standard model of particle physics is today our basic theory of fundamental particles, and their interactions. The model incorporates three of the fundamental forces, the strong, the electromagnetic and the weak force. The elementary particles can be classified into groups called leptons and quarks (spin $\frac{1}{2}$ fermions), and the gauge bosons which are the force carriers (spin 1 particles). The strong force is responsible for binding quarks together into hadrons, while the electromagnetic force is responsible for the interaction between electric charges (binding of electrons to nuclei in atoms). The weak force is responsible for processes like β-decay.

2.1   Leptons and Quarks

There are three families of quarks and leptons, each with increasing mass, but only the first family is considered stable. The first family consists of the lepton electron (e) and the electron neutrino (ν_e), and the quarks up (u) and down (d). The second family consists of the lepton muon (μ) and the muon neutrino (ν_μ), and the quarks charm (c) and strange (s). The third family consists of the lepton tau (τ) and the tau neutrino (ν_τ), and the quarks top (t) and bottom (b). To each particle there exists an anti-particle, where the anti-particle will have the same properties as the particle, but opposite charge.

The quarks build up hadrons, which are divided into two classes, the baryons (half integer spin) and the mesons (integer spin). A baryon consist of three quarks, while a meson consists of a quark and an anti-quark. Quarks carry an extra degree of freedom, a color charge (red, green, and blue). Hadrons have no color charge, making the quarks that build them

3

Table 2.1: Leptons in the standard model, with some important quantum numbers. In the standard model neutrinos have no mass, but evidence for neutrino masses exist from observation of neutrino oscillations. Neutrinos masses are given by the upper limit from [2]. These data are based on PDG (Particle Data Group) 2008 information [3].

Leptons					
Name	Mass	Charge	Isospin		Hypercharge
l	(MeV/c^2)	(Q)	(I)	(I_3)	(Y)
Electron(e^-)	~ 0.511	-1	$\frac{1}{2}$	$-\frac{1}{2}$	-1
ν_e	$< 2 \cdot 10^{-6}$	0	$\frac{1}{2}$	$\frac{1}{2}$	-1
Muon(μ^-)	~ 105.658	-1	$\frac{1}{2}$	$-\frac{1}{2}$	-1
ν_μ	<0.19	0	$\frac{1}{2}$	$\frac{1}{2}$	-1
Tau(τ^-)	~ 1776.990	-1	$\frac{1}{2}$	$-\frac{1}{2}$	-1
ν_τ	<18.2	0	$\frac{1}{2}$	$\frac{1}{2}$	-1

up to be of color neutral combination. Thus mesons are color anti-color combinations while baryons are combinations of three different colors, thus giving a neutral color combination.

Table 2.2: Quark content in the standard model with some important quantum numbers. These data are based on PDG 2008 information.

Quarks					
Name	Mass	Charge	Isospin		Hypercharge
q	(MeV/c^2)	(Q)	(I)	(I_3)	(Y).
Up (u)	$1.5 \sim 3.3$	$\frac{2}{3}$	$\frac{1}{2}$	$\frac{1}{2}$	$\frac{1}{3}$
Down (d)	$3.5 \sim 6.0$	$-\frac{1}{3}$	$\frac{1}{2}$	$-\frac{1}{2}$	$\frac{1}{3}$
Charm (c)	1270^{+70}_{-110}	$\frac{2}{3}$	$\frac{1}{2}$	$\frac{1}{2}$	$\frac{1}{3}$
Strange (s)	104^{+26}_{-34}	$-\frac{1}{3}$	$\frac{1}{2}$	$-\frac{1}{2}$	$\frac{1}{3}$
Top (t)	$(171.2 \pm 2.1) \cdot 10^3$	$\frac{2}{3}$	$\frac{1}{2}$	$\frac{1}{2}$	$\frac{1}{3}$
Botton (b)	$\left(4.20^{+0.17}_{-0.07}\right) \cdot 10^3$	$-\frac{1}{3}$	$\frac{1}{2}$	$-\frac{1}{2}$	$\frac{1}{3}$

Tables 2.1 and 2.2 list the quantum numbers for the weak isospin (I) and the third component of weak isospin (I$_3$), for left handed fermions. The weak hypercharge is directly related to the charge and the third component of isospin by the Gell-Mann-Nishijima formula [4]

$$Q = \frac{Y}{2} + I_3 \,. \tag{2.1}$$

2.2 Gauge Bosons

Gauge bosons are known as force mediating particles. The gluons (g) mediate the strong force, the photon (γ) mediates the electromagnetic force, while the Z^0 and $W^\pm$ mediate the weak force. Table 2.3 gives some details for the gauge bosons. The coupling constant are known as running couplings, because their numerical value changes with energy.

Table 2.3: The fundamental forces in nature and their mediating particles. Gravity is not included in the standard model.

Force	Range (m)	Strength	Mediator	Coupling constant
Electromagnetic	Infinite	$\frac{1}{137}$	Photon	α_1
Weak	$\sim 10^{-18}$	10^{-6}	$W^\pm$, Z^0	α_2
Strong	$\sim 10^{-15}$	1	Gluons	α_3
Gravitational	Infinite	10^{-39}	Graviton	-

2.3 The Standard Model Gauge Group

The mathematical description of the standard model is the gauge invariant theory of $SU(3)_C \times SU(2)_L \times U(1)_Y$, which is commonly called the Standard Model. QCD describes the strong interaction which is represented with $SU(3)_C$, where C denotes color. $SU(2)_L \times U(1)_Y$ is the electroweak part of the standard model, which is the unified theory for the weak and the electromagnetic forces. Left handed fields transform as doublets under $SU(2)_L$, while right handed fields transform as singlets and Y is the hypercharge.

2.4 The Higgs Mechanism

In the standard model, fermions and gauge bosons acquire masses via their interaction with a Higgs field. In the simplest case this is achieved by introducing an SU(2) scalar doublet field. Its self-interactions provide the necessary mechanism for spontaneous symmetry breaking. Spontaneous symmetry breaking of $SU(2) \times U(1)$ symmetry and gauge invariance, give masses to the gauge bosons, while the Yukawa couplings give masses to the fermions. In the simplest scenario this gives one massive particle, the Higgs particle. Search for the Higgs particle is one of the main priorities of the Large Hadron Collider.

2.5 Physics beyond the Standard Model

Although the standard model gives a good description of low energy phenomena, it fails to describe the large difference in the coupling constant. The Grand Unified Theory (GUT) suggests that the standard model groups $SU(3)_C$, $SU(2)_L$ and $U(1)_Y$ are subgroups of a larger symmetry group called, G. GUT suggests that symmetries are unbroken above a certain very large mass scale, M_X. Above this mass scale M_X, the coupling constant can be related to a single gauge coupling. Below the GUT scale, symmetries become spontaneously broken, and the coupling constants evolve separately.

An extension to the standard model is the concept of supersymmetry. It introduces a symmetry between fermions and bosons. Its algebra consists of both commutation and anti-commutation relations. Supersymmetry in its simplest form is a self-conjugate spin $\frac{1}{2}$ Majorana generators Q_α, that turns boson fields into fermion fields, and vice versa. Supersymmetry provides us with supersymmetric partner to all the standard model particles, the squarks, sleptons, gauginos and the higgssinos [5]. Supersymmetric particles have not yet been discovered, but is a popular theory for physics beyond the standard model.

Another theory for physic beyond the standard model is the theory of superstring. Attempts to unify all fundamental forces and include theory of quantum gravity is found in superstring theory. The relevant scale for this unification is at the planck scale. Here all fundamental objets are 1-d dimensional strings, with dimensions of length. Vibration of the sting gives the particles flavor, charge, mass and spin. All masses, couplings and other properties are in principle predictable in superstring theory.

Chapter 3

Black Holes

Physics beyond the standard model scenarios which include extra space dimensions, offer a new way to solve outstanding problems in the standard model. In these models, the Planck scale gets reduced to the order of the electroweak symmetry breaking scale. One exiting consequence of these models, is that mini black holes may form in particle physic experiments, like those at the LHC.

3.1   Hierarchy Problem

The hierarchy problem is one of the major questions in particle physics. It refers to the following question; Why is the observed gravity so weak compared to the other forces of nature (strong, weak, electromagnetic)? Attempts to unify gravity with the other forces, becomes problematic due to the enormous energy gap between the electroweak symmetry breaking scale ($M_{EW} \sim 10^3\,\text{GeV}$) and the scale where gravity is expected to become as strong as the other forces. This is known as the Planck scale (M_{Pl})

$$M_{Pl} = \sqrt{G_N} \approx 1.22 \cdot 10^{16}\,\text{TeV}\,, \tag{3.1}$$

where G_N is the Newton gravitational constant. We will now discuss some extra dimensional scenarios, where the observed Planck scale is not the fundamental energy scale, but rather a consequence of being observed by a 3 dimensional observer.

3.2   ADD scenario

In 1998 Nima Arkani-Hamed, Savas Dimopoulos and Gia Dvali [6] proposed a scenario involving large extra spatial dimensions. The motivation for this scenario was to solve the hierarchy problem. In the ADD scenario, one assumeds that there exists n extra compact spatial dimensions. These extra dimensions have a radius R, and the Planck scale $M_{Pl(4+n)}$ in this $(4 + n)$ dimensional theory is of the order of $\sim M_{EW}$.

The relationship between the four dimensional Planck (M_{Pl}) scale and the $M_{Pl(4+n)}$ can be derived by using Gauss law. If two test masses m_1 and m_2 are placed at a distance from each other $r \ll R$, the gravitational potential they feel is

$$V(r) \sim \frac{m_1 m_2}{M_{Pl(4+n)}^{n+2}} \frac{1}{r^{n+1}} . \tag{3.2}$$

If the two test masses were placed at a distance $r \gg R$, the gravitational potential changes to

$$V(r) \sim \frac{m_1 m_2}{M_{Pl(4+n)}^{n+2} R^n} \frac{1}{r} . \tag{3.3}$$

By comparing the last equation to Newtons gravitational potential, one finds the relationship between M_{Pl} and $M_{Pl(4+n)}$.

$$M_{Pl}^2 \sim M_{Pl(4+n)}^{2+n} R^n . \tag{3.4}$$

The size of this extra dimension can then be calculated. If $n = 1$ the size of the extra dimension is of the order $R \sim 10^{11}$ m, but if $n = 2$ the radius is of the order of $R \sim 100\,\mu$m. With increasing numbers of extra dimensions the size of these dimensions are decreasing, thus explaining why they are not discovered yet. Later, we will refer to $M_{Pl(4+n)}$ as M_D.

The current 95% C.L. on the planck scale M_D has been set by using the data from CDF II detector, which used $p\bar{p}$ collision with a center of mass energy of $\sqrt{s} = 1.96$ TeV. It used $\gamma + E_T$ (jet+E_T) with and integrated luminosity of 2.0 fb^{-1} (1.1 fb^{-1}) to set combined limits at $M_D < 1.4$ TeV ($M_D < 0.940$ TeV) for n=2 (n=6) [7].

3.3   The Randall-Sundrum model (RS)

Another way of solving the hierarchy problem was proposed by Lisa Randall and Raman Sundrum [8]. It relies on the existence of one compact extra dimension. To achieve this, one places two 3-dimensional branes with equal and opposite tensions at fixed points S_1/Z_2, in a five dimensional anti-deSitter space-time (AdS_5). Anti-de Sitter space is the maximally

symmetric solution of Einsteins field equation with an attractive cosmological constant. The given metric for this AdS_5 is

$$ds^2 = e^{-2kr_c\phi}\eta_{\mu\nu}dx^\mu dx^\nu + r_c^2 d\phi^2 \,, \tag{3.5}$$

where $0 \leq |\phi| \leq \pi$ is the coordinate along the compact dimension of radius r_c. The parameter k is referred to as the warp factor, (it is the curvature of the AdS_5), $\eta_{\mu\nu}$ is the metric tensor and x^μ are the normal (3+1) space-time coordinates. One of these branes are known as the Planck brane, placed at $\phi = 0$. Gravity originates from this Planck brane. The other brane is the standard model brane, which is located at $\phi = \pi$. In this scenario, gravity will become exponentially suppressed away from the Planck brane, along the fifth dimension, due to the warp factor,

$$\Lambda_\pi = \bar{M}_{Pl}e^{-\pi kr_c}, \tag{3.6}$$

where $\bar{M}_{Pl}$ is the reduced Planck mass, $\bar{M}_{Pl} = M_{Pl}/\sqrt{8\pi}$. The hierarchy between the electroweak and the Planck scale can be removed if $\Lambda_\pi \sim 1$ TeV. This can be achieved if $kr_c \approx 12$. One often introduces a dimensionless parameter $\widetilde{k} \equiv k/\bar{M}_{Pl}$, which represents the strength between the standard model fields and the graviton.

In the simplest RS model, gravitons are the only particles that are allowed to propagate in the extra dimensions. As a consequence they appear as massive Kaluza-Klein (KK) modes, and can be produced in $p - p$ collisions. In the RS model the KK tower will decay to fermion-antifermion pairs or diboson pairs. These towers will give a characteristic resonance structure in the invariant mass spectrum. Only the zero mode remains massless and couples to the standard model fields as $1/M_{Pl}$, while the exited mass modes couple to the standard model fields with strength $1/\Lambda_\pi$. CDF and DØ have searched for these modes using dimuon, dielectron, and diphoton channels. They have set the current upper limits at 95% CL limits of $1/\Lambda_\pi < 4.3$ (2.6) TeV for $m_1 = 500$ (700) GeV [9, 10], where m_1 is the first exited mass state for the KK tower.

3.4 Black Holes in large extra dimensions

For an object to become a black hole, the mass of the object has to be compressed into a sphere with radius R$_S$. This solution was first obtain by Karl Schwarzschild, thus known as the Schwarzschild radius. For a four dimensional object the solution for the Schwarzschild radius was found by applying general relativity to a static non-spinning massive object

$$R_S = 2\frac{GM}{c^2} \,, \tag{3.7}$$

where G is the gravitational constant, M is the mass of the object and c is the speed of light. Equation 3.7 can be used to calculate the Schwarzschild radius for all four dimensional objects. For the earth the Schwarzschild radius is approximately 1 cm, while for the

sun it is approximately 3 km.

In the case of large extra dimensions, the solution for Schwarzschild radius changes to [11]

$$R_{BH} = \frac{1}{M_D} \left(\frac{M_{BH}}{M_D} \right)^{\frac{1}{n+1}} f(n), \tag{3.8}$$

with

$$f(n) = \left(\frac{2^n \pi^{\frac{n-3}{2}} \Gamma \left(\frac{n+3}{2} \right)}{n+2} \right)^{\frac{1}{n+1}}, \tag{3.9}$$

where M_{BH} is the mass of the black hole, n is the number of extra dimensions, M_D is the Planck scale in $(4+n)$ dimensions and $\Gamma(x)$ is the gamma function. In order to fulfill a thermodynamic description the black hole must have an entropy greater then 25, leading to the requirement that the mass of the black hole must satisfy $M_{BH} > 5M_D$ [12].

The Schwarzschild radius is an important factor in the creation of a black hole, considering two partons traveling towards each other, with a center of mass energy of $\sqrt{\hat{S}} \geq M_{BH}$. If the colliding partons pass within a distance of r$< R_S$, a black hole may form with mass M_{BH}. The parton level cross section for creation of a black hole in $(n+4)$ dimensions, can be approximated by geometrical arguments as [12]

$$\hat{\sigma}(M_{BH}) \approx \pi R_S^2 = \pi \frac{f^2(n)}{M_D^2} \left(\frac{M_{BH}}{M_D} \right)^{\frac{2}{n+1}}. \tag{3.10}$$

Figure 3.1 a, b, shows the parton cross section, as well as the differential production cross section produced at the LHC. For n=4, and M_{BH}= 5 TeV, we expect the parton cross section to be in the order of ~ 10 pb.

3.4.1   Black Hole Evaporation

Classically, black holes do not emit particles, only absorb them. But Steven Hawking showed that black holes can evaporate by emitting Hawking radiation [14]. Hawking found that the black hole radiation spectrum is almost like a black body radiation spectrum. It is categorized by the Hawking temperature

$$T_H = \frac{\hbar c}{4\pi k r_S}, \tag{3.11}$$

where k is the Boltzmann constant. For later references, natural units are used; $c = \hbar = k = 1$.
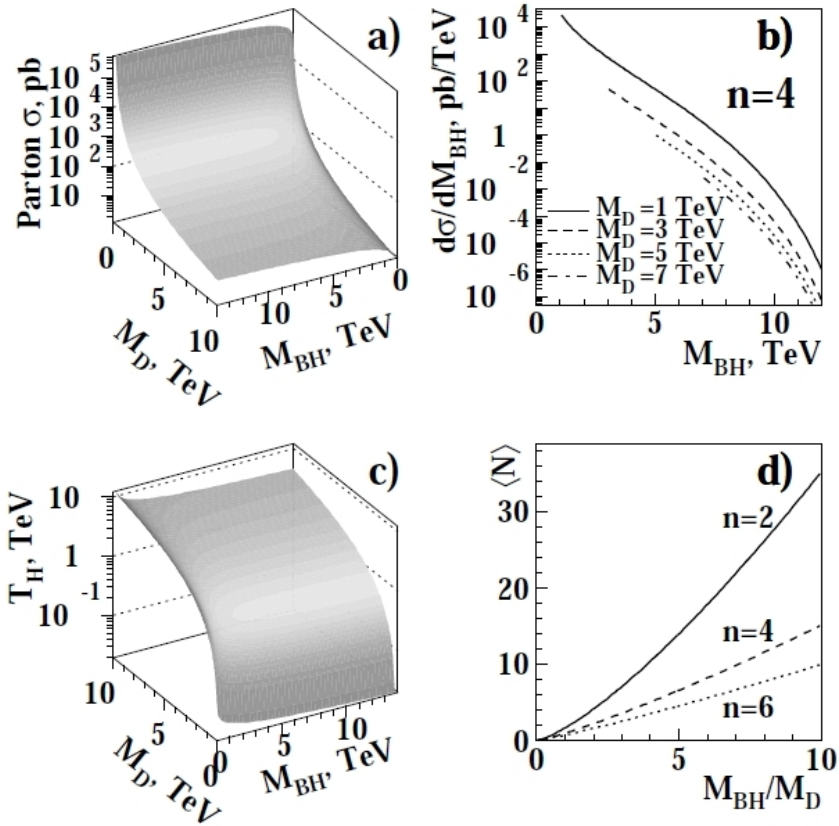
Figure 3.1: a) Parton level cross section. b) Differential production cross for *pp* collision. c) Hawking temperature. d) Average number of decay products. a)-c) Assumed that the number of extra dimensions is n=4. a)-b) Made with a center of mass energy of 14 TeV, from [13].

It is expected that a black hole produced at the LHC will decay almost instantaneously, with a life time of the order of $10^{-27}s \sim 10^{-26}$ s [15]. In this short life time, one expects a black hole to go through four phases [16, 17].

- *Balding phase:* When a black hole is formed, it first enters a stage where energy is lost via emission of gauge and gravitational radiation. At the end of this phase the final state is a black hole with no 'hair'. This refers to the fact that only the observable quantities for an external observer are mass, electric charge and angular momentum. It is estimated that the black hole looses 16% of its energy in this phase.

- *Spin-down phase:* Due to the conservation of angular momentum, the black hole is expected to be formed with non-zero angular momentum. In this phase the black

hole looses energy via Hawking radiation of quanta that preferentially have an angular momenta of $l \sim 1$. It is expected that a black hole looses about 25% of its energy in this phase.

- *Schwarzschild phase:* The black hole continues to loose its energy via Hawking radiation. As a result, the mass is gradually decreasing while the Hawking temperature is increasing.

- *Planck phase:* When the mass of a black hole reaches a mass M $\sim$ M$_P$, Hawking calculations fail, because the last stage of a black hole life is fairly unknown, since quantum gravity becomes important, but it is expected that the black hole will decay into a few fundamental particles like: q, l, ν, γ, g, W, Z and H.

The average number of particles produced in a black hole decay can be estimated from the Hawking temperature, as a function of numbers of dimensions. Note that this argument is based on the assumption that the decay of a black hole is a blackbody radiation process [13]. The Hawking temperature can be expressed as

$$T_H = \left(\frac{M_D}{M_{BH}} \frac{n+2}{8\Gamma\left(\frac{n+3}{2}\right)} \right)^{\frac{1}{n+1}} \frac{n+1}{4\sqrt{\pi}} = \frac{n+1}{4\pi R_S} . \tag{3.12}$$

The average number is then given by

$$< N > \approx \frac{M_{BH}}{2T_H} = \frac{2\sqrt{\pi}}{n+1} \left(\frac{M_{BH}}{M_{D(4+n)}} \right)^{\frac{n+2}{n+1}} \left(\frac{8\Gamma\left(\frac{n+3}{2}\right)}{n+2} \right)^{\frac{1}{n+1}} . \tag{3.13}$$

In Figure 3.1 c, d, the Hawking temperature, as well as the number of decay product is shown as a function of M$_D$, M$_{BH}$ and number of dimensions.

3.5 RS Black Hole

Black holes can also be produced in the RS scenario, and will be quite similar to that of black hole production in ADD with n=1 [15]. Here one defines a five dimensional Plank scale M, and relates this to the reduced four dimensional Planck scale by [15]

$$\bar{M}_{Pl} = \frac{M^3}{k} \left(1 - e^{-2\pi k R_c} \right) \approx \frac{M^3}{k} . \tag{3.14}$$

The Schwarzschild radius for a RS black hole is

$$R_S = \frac{1}{\pi M e^{-\pi k R_c}} \sqrt{\frac{M_{BH}}{3 M e^{-\pi k R_c}}} \ . \tag{3.15}$$

3.6 Black Hole Event Properties

To discover black holes in particle physics experiments, the approximate signature looked at, is this high mass scale. The high mass scale combined with its thermal decay process results in a large number of high p_T final state particles. The resulting objects range between all standard model particles, also including the Higgs particle. Emission of graviton is also expected, thus resulting in a contribution to the missing energy. From Equation 3.13 one finds that for increasing Hawking temperature the number of decay products is decreasing, thus resulting more energetic decay products.

3.7 String Balls

If we assume a scenario which includes large extra spatial dimensions, and then if $M_D >$ 1TeV, and the requirement for a black hole in the context of the requirement from general relativity (GR) $M_{BH} > 5M_D$ [12], this may lead to the case that black hole production is out of reach to the energies at the LHC. The range between M_D and the GR threshold for creating a black hole, can be treated in the context of weakly coupled string theory.

When a black hole evaporates, the mass of the black hole gets gradually reduced. When it crosses the GR threshold, according to string theory, it can make the transition into weakly couples string state, known as string balls. The relationship between the M_D and the string scale M_S can be obtained by

$$M_D^{n+2} \sim \frac{M_S^{n+2}}{g_s^2}, \tag{3.16}$$

where n is the number of large extra dimensions, and g_s is the string coupling. For string theory to be perturbative, $g_s < 1$. One finds that $M_D > M_S$ for all n. According to string theory, the minimum mass of a black hole that can be treated as a GR object yielding

$$M_{min} \sim \frac{M_S}{g_s^2} \ . \tag{3.17}$$

At this energy scale, the properties for a black hole with mass M_{min} has to match those of a string ball with the same mass. The minimum mass requirement for string ball production,

is $M_{SB} > 3M_S$ [12]. The parton level cross section for a string ball has to match that of a black hole at M_S/g_s^2. The production of string balls and black holes depend on M_S, g_s, n and M_D, where

$$M_S < M_D < \frac{M_S}{g_s} < \frac{M_S}{g_s^2} \, . \tag{3.18}$$

The parton cross section is given as a function of the mass range (M) [12]

$$\hat{\sigma} = \frac{g_s^2 M^2}{M_s^4} \qquad\qquad M_S \ll M \le \frac{M_S}{g_s} \tag{3.19}$$

$$\hat{\sigma} = \frac{1}{M_S^2} \qquad\qquad \frac{M_S}{g_s} \le M \le \frac{M_S}{g_s^2} \tag{3.20}$$

$$\hat{\sigma} = \pi \frac{f^2\left(n\right)}{M_D^2} \left(\frac{M}{M_D}\right)^{\frac{2}{n+1}} \qquad\qquad \frac{M_s}{g_s^2} < M \tag{3.21}$$

and The first two equations show the string ball cross sections, while the last equation represent the previouslt stated back hole cross section in Equation 3.10. Figure 3.2 shows
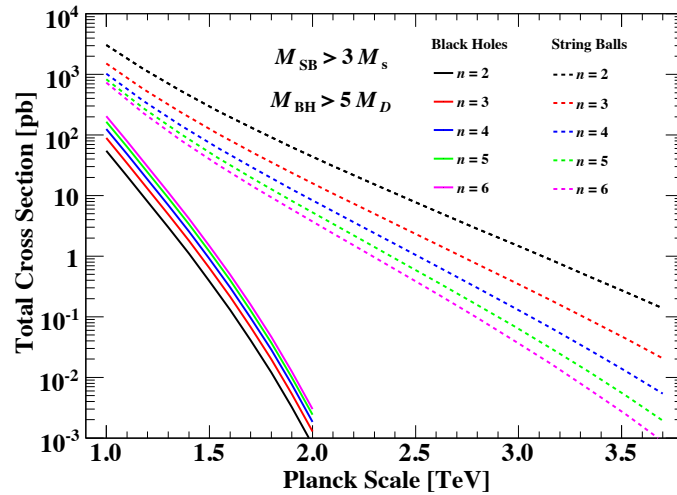

Figure 3.2: Total proton-proton cross section versus planck scale, M_D, for black hole and string ball production. Assuming that $M_{SB} > 3M_S$ and $M_{BH} > 5M_D$. Various scenarios of extra dimensions n is shown [12].

the production cross section of string balls and black holes as a function of the planck scale (M_D). The center of mass energy of the colliding protons was assumed to be 14 TeV. For a string ball production, in $n = 6$ extra dimensions and M_D=1.3 TeV, the production cross section is of the order of ~ 100 pb.

Once a string ball has been formed, it will decay into massless and massive particles. By averaging over all string excitations, one finds that the radiation spectra from a string

evaporation is a black body radiation spectra, characterized by the Hagedorn temperature [18]. The Hagedorn temperature is given by

$$T_S = \frac{M_S}{\sqrt{8\pi}} \, . \tag{3.22}$$

The average number of decay products is approxamently the mass divided by the Hagedorn temperature (M/T_S) [19]. It is expected that a string ball will decay into all types of standard model particles with equal probability. The result of this is that approximately 10% of the decay products will be charged leptons, and 2% will be photons.

Chapter 4

The ATLAS Experiment

To gain a better understanding of the elementary particles and the forces between them, particle accelerators and detectors are used. This chapter will give a short description of the Large Hadron Collider (LHC) and a more detailed description of the ATLAS (A Toroidal LHC ApparatuS) detector.

4.1   CERN

The European Organization for Nuclear Research CERN (Conseil Europen pour la Recherche Nuclaire) is the largest particle physics laboratory in the world. It is located on the French-Swiss border, near the city of Geneva. CERN was founded in 1954 and consists today of 20 member states. Form the first accelerator the Synchrocyclotron to the Large Hadron Collider, CERN has made some remarkable contributions to science and technology.

4.2   LHC

The Large Hadron Collider (LHC) is located in the old LEP tunnel, which crosses the border between France and Switzerland. It is located below ground, varying from 175 m under Jura mountains, to about 50 m towards Lake Geneva. The LHC is a storage ring, in which protons collide with protons at a center of mass energy of 14 TeV. The LHC can also collide heavy ions (A), at an energy of 5.5 TeV per nucleon pair. But only proton-proton collision will be discussed further here. Four experiment operate simultaneously at the LHC. There are two multipurpose experiments: ATLAS and CMS (Compact Muon

Solenoid). A dedicated B-physic experiment: LHCb. There is also an experiment dedicated to heavy ion collisions: ALICE.

The number of events per second created by the LHC collisions, is given by

$$N_{event} = \mathscr{L}\sigma_p\,, \tag{4.1}$$

where $\mathscr{L}$ is the luminosity for the machine, and σ_p is the cross section for the process under study. The luminosity is only dependent on the machine properties. The luminosity can be calculated from the number of particles per bunch (N_b), the number of bunches per beam n_b, the revolution frequency f_{rev} and the horizontal and vertical beam sizes (σ_x, σ_y),

$$\mathscr{L} = \frac{1}{4\pi}\frac{n_b f_{rev} N_b^2}{\sigma_x \sigma_y}. \tag{4.2}$$

For proton-proton collisions the design luminosity is $10^{34}\,\mathrm{cm^{-2}s^{-1}}$, which corresponds to an integrated luminosity of 100 fb^{-1}. Figure 4.1 shows the expected cross section for different
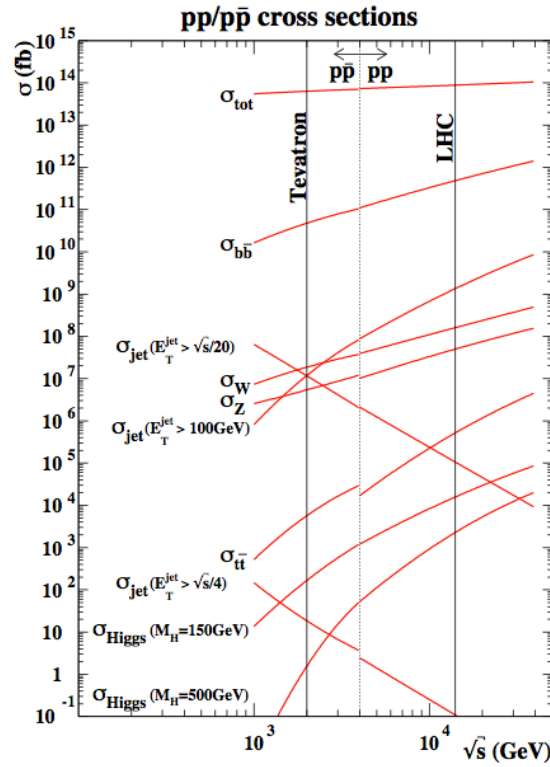

Figure 4.1: Shows the cross section for different processes as a function of $\sqrt{s}$, from [20].

standard model processes, as a function of $\sqrt{s}$. Note that the low energy scale cross section is for the Tevatron, which is a proton anti-proton collider experiment, at fermi lab. The thin dotted line is indicating the change between proton anti-proton and proton-proton collisions, which is the case for the LHC experiment.

4.2.1 The LHC Injection Chain

In order to accelerate the protons up to the design center of mass energies, the LHC needs several pre-accelerators. Each of them is designed to increase the energy, before sending the beam to the next accelerator. Figure 4.2 illustrates the accelerator structure that is used. First, a linear accelerator (LINAC2) accelerates protons to 50 MeV. Before sending them to the booster, a synchrotron, that accelerates them to 1.4 GeV. The beam is the injected into the Proton Synchrotron (PS) that accelerates them to 25 GeV. Next the protons are sent to the Super Proton Synchrotron (SPS) which provides acceleration to 450 GeV before the protons enter the 27 km long LHC tunnel [21]. Here the protons are accelerated there final energy. Though the maximum beam energy is 7 TeV, in the first period of data taking 2010/2011, the protons will collide with a beam energy of 3.5 TeV.
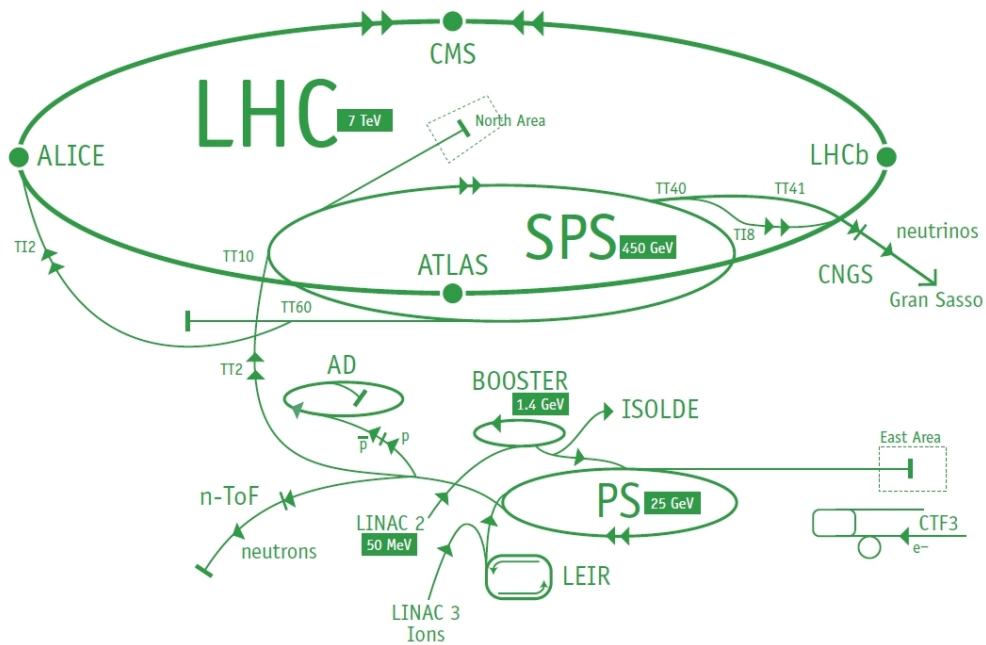

Figure 4.2: The LHC Injection Chain [21]

4.3 The ATLAS Detector

The ATLAS detector consist of three main sections. Inside a solenoid lies the inner detector, providing tracking information. On the outside of the solenoid are the electromagnetic and hadronic calorimeters, providing energy measurement. In the outer layers is the muon
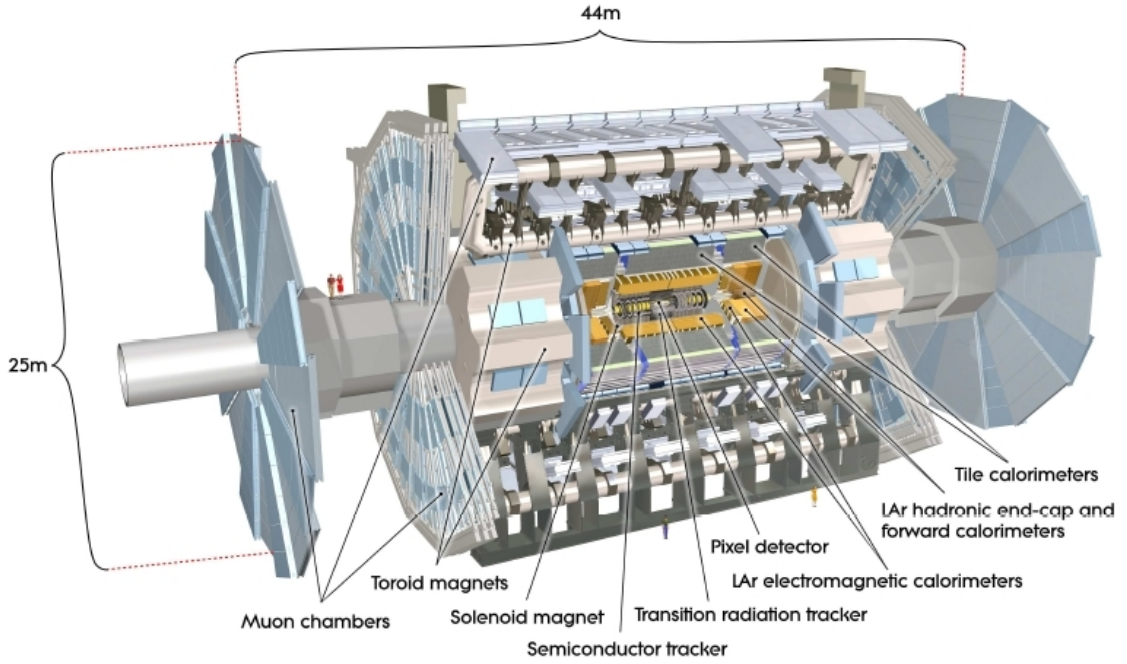
Figure 4.3: Overview of the ATLAS Detector

spectrometer, placed in a toroid magnetic field. Figure 4.3 shows a three-dimensional illustration of the ATLAS detector. Including the muon chamber endcaps, the ATLAS detector is approximately 44 m long and 25 m high, and weights about 7000 tonnes. In table 4.1 the performance goals of the ATLAS detector is shown. The layout and expected performance of the ATLAS detector was extracted from referance [22], unless stated otherwise.

Table 4.1: General performance goals for the ATLAS detector. All units for E and p_T are in GeV.

Detector component	Required resolution	η coverage	
		Measurement	Trigger
Tracking	$\sigma_{p_T}/p_T = 0.05\%p_T \oplus 1\%$	± 2.5	
EM calorimeter	$\sigma_E/E = 10\%/\sqrt{E} \oplus 0.7\%$	± 3.2	± 2.5
Hadron calorimeter			
barrel and endcap	$\sigma_E/E = 50\%/\sqrt{E} \oplus 3\%$	± 3.2	± 3.2
forward	$\sigma_E/E = 100\%/\sqrt{E} \oplus 10\%$	$3.1 < |\eta| < 4.9$	$3.1 < |\eta| < 4.9$
Muon spectrometer	$\sigma_{p_T}/p_T = 10\%$ at $p_T = 1\text{TeV}$	± 2.7	± 2.4

4.3.1 ATLAS Geometry

The geometric layout of the ATLAS detector is a right handed coordinate system. The origen is placed in the interaction point. The z-axis points along the beam direction. The positive x-axis points towards the center of the LHC ring and the positive y-axis points up towards the surface. The azimuthal angle (ϕ), is defined as

$$\phi \equiv \tan^{-1}\left(\frac{p_y}{p_x}\right), \tag{4.3}$$

where p_x and p_y are the x and y-components of the particle momentum. The pseudorapidity (η) is defined as

$$\eta = -\ln\left(\tan\left(\frac{\theta}{2}\right)\right), \tag{4.4}$$

where θ is the angle between the beam axis and the particle, for relativistic particles the pseudorapidity is a good approximation of the rapidity, difiend by

$$y = \frac{1}{2}ln\left(\frac{E + p_L}{E - p_L}\right), \tag{4.5}$$

where E is the energy of the particle, and p_L is the momentum parallel to the beam axis. The transverse momentum is a often used observable in ATLAS, it is the momentum orthogonal to the beam direction,

$$p_T = \sqrt{p_x^2 + p_y^2}. \tag{4.6}$$

E_T is the energy deposit in the transverse plane, compared to the beam direction. $\not{E}_T$ is the missing energy in the transverse plane. Missing energy comes from conservation of energy. Before collision the proton carry only momentum in the longitudinal direction, so $p_T = 0$. After collision particles have momentum in all directions. Do to momentum conservation $\sum p_T = 0$. Contribution to the missing energy comes form particles that is not discovered by the detector, such as neutrinos, and from the detector geometry.

4.3.2 The Inner Detector

Located closest to the interaction point, is the inner detector (ID). Figure 4.4 shows a illustration of the ID and its sub systems, while Figure 4.5 shows a two dimensional projection of the ID, indicating the regions it covers. Figure 4.6 shows how the inner detector elements are placed in R direction, with respect to each other. There are three subdetectors: the Pixel Detector (PD), Semi Conductor Tracker (SCT) and the Transition Radiation Tracker (TRT). The ID is designed to provide primary and secondary vertex measurements. It covers $|\eta| < 2.5$, and gives an excellent momentum resolution for charged particles with a transverse momentum $p_T > 0.5\,\text{GeV}$.
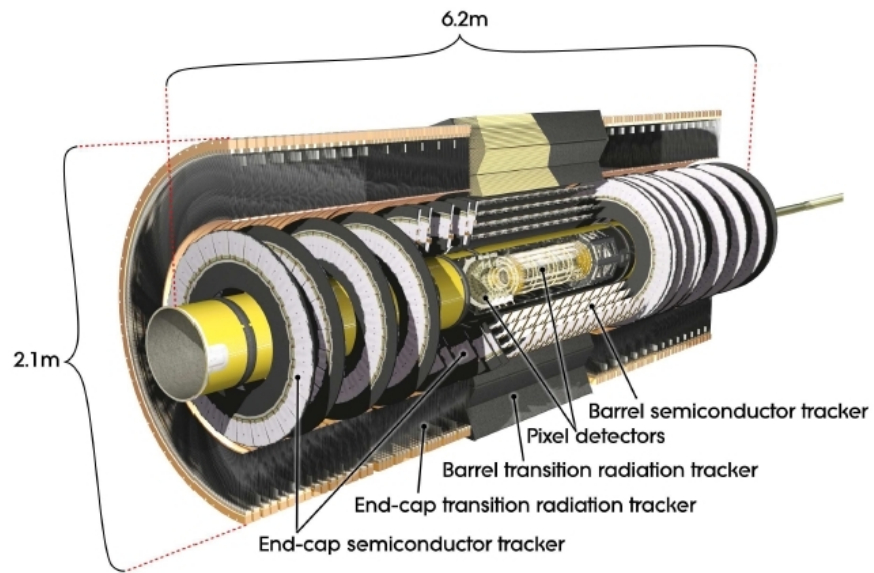
Figure 4.4: The ATLAS inner detector, showing all major detector elements of the inner detector.
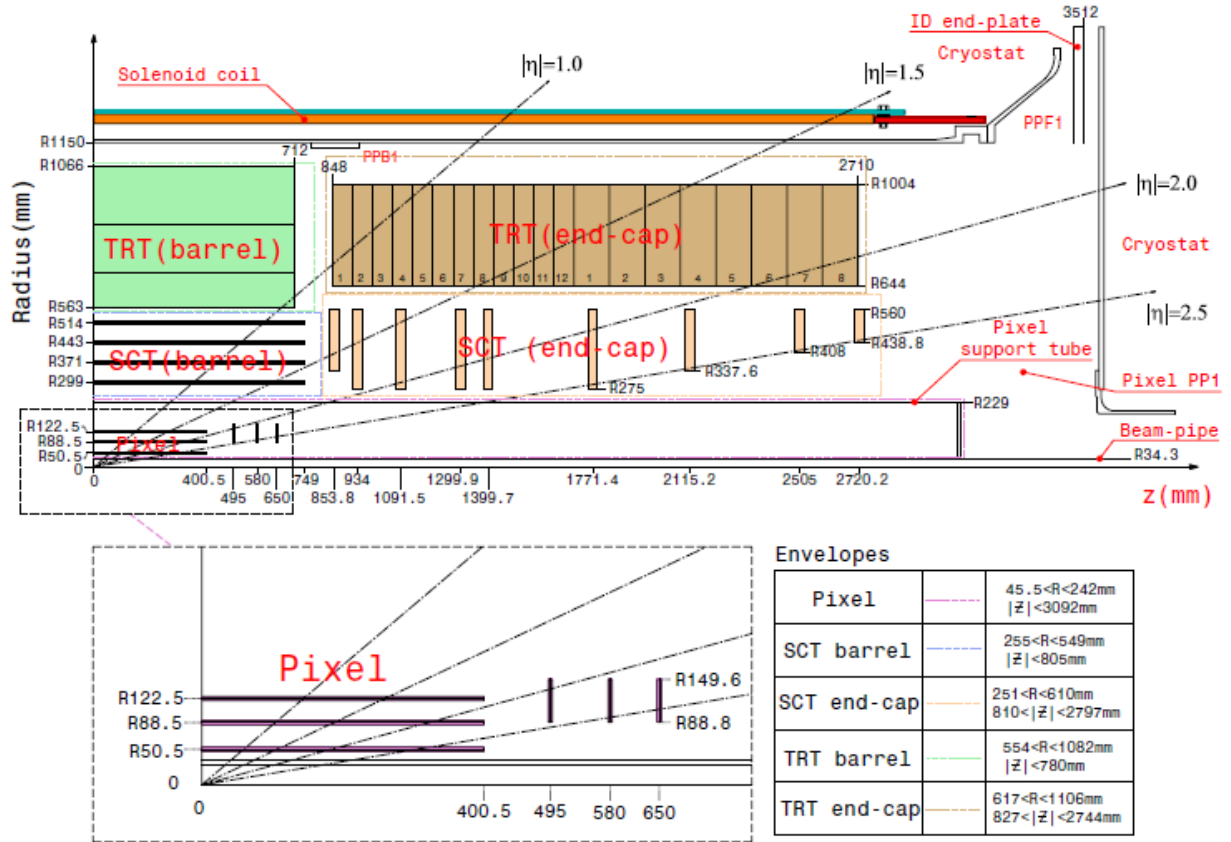
Figure 4.5: Plane view of a quadrant of the ATLAS inner detector, showing all major detector elements, in R and Z position. The η coverage of the individual elements is shown by the dashed lines.

The Pixel Detector

The PD is the inner most detector, containing 1744 identical pixel sensors, with external dimensions of 19×63 mm^2. The pixel sensors are arranged in three cylindrical layers in a barrel and three endcap disks on each side. It covers a region of $|\eta| < 2.5$. For 90% of the pixels the dimensions are $50 \times 400 \mu$m^2, while for the remaining 10% they are $50 \times 600 \mu$m^2. The intrinsic position resolution in the barrel is 10 μm $(R - \phi)$ and 115 μm (z), in the endcaps it is 10 μm $(R - \phi)$ and 115 μm (R).
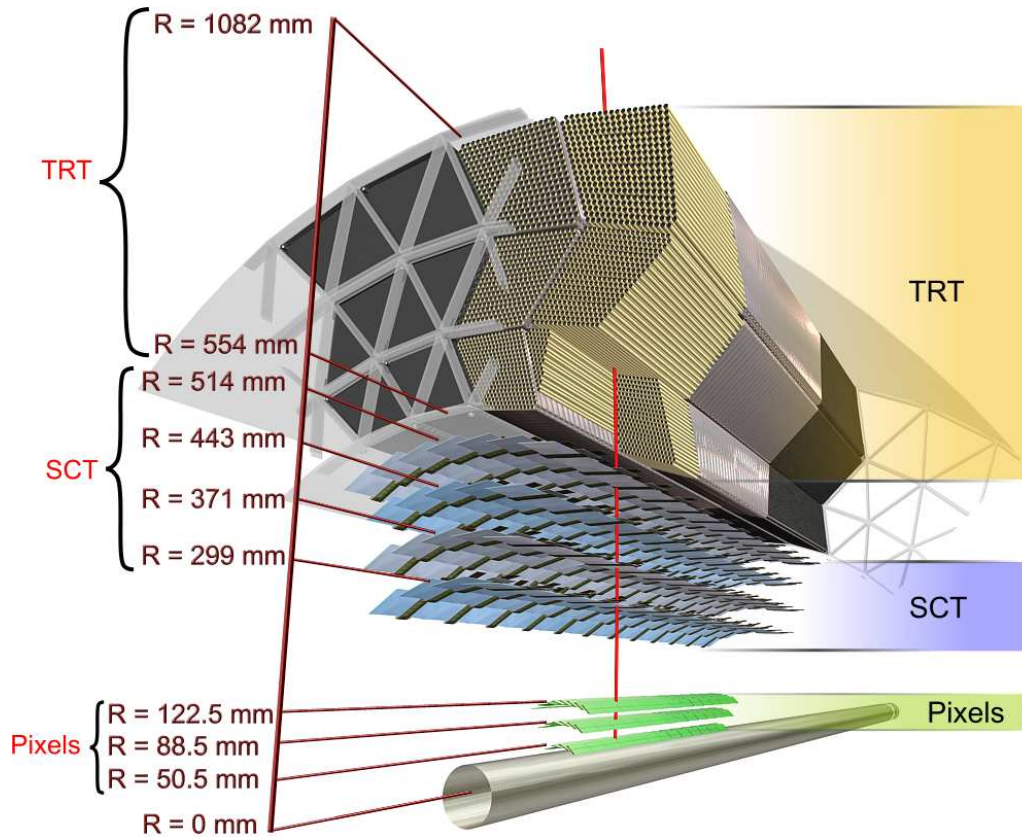
Figure 4.6: Three-dimensional layout of the different subdetectors of the ID.

The SemiConductor Tracker (SCT)

The SCT consists of four double-layers barrels and two end-caps, each consisting of nine disks. Built from 4088 modules, it covers $|\eta| < 2.5$. Thus, at least four space points are measured. The SCT consists of silicon microstrips. The double-layer barrels are arranged with one layer being parallel to the beam direction, while the other layer is rotated by an angle of ± 20 mrad, providing both $(R - \phi)$ and (z) measurements. The silicon microstrips in the end-cap is arranged in the radial direction, compared to the beam direction. The end-caps disks consist of nine disks of back-to-back silicon microstrips, where one is rotated by an angle of ± 20 mrad, giving measurement in both $(R - \phi)$ and (R). The intrinsic resolution in the barrel is 17 μm $(R - \phi)$ and 580 μm (z) and in the disks 17 μm $(R - \phi)$, and 580 μm (R).
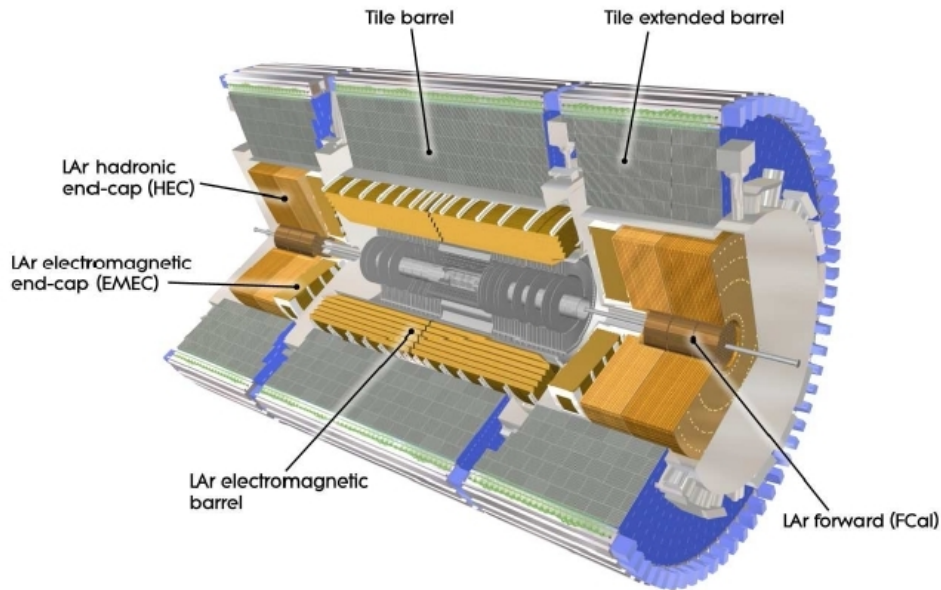
Figure 4.7: The ATLAS calorimeters

The Transition Radiation Tracker (TRT)

The TRT consists of 52 446 Polymide drift tubes (straw), that are stacked in three cylindrical layers in a barrel, with the straws being parallel to the beam direction. Each endcap consists of 122 880 straws that are placed radiantly in wheels, compared to the beam direction. Each tube has a radius of 0.4 cm. In the barrel (end-cap) the straws have a length of 144 cm (37 cm). The drift tubs are filled with a gas mixture of 70% Xe, 27% CO_2 and 3% O_2, covering the pseudorapidity of $\eta < 2.0$. Charged tracks in $\eta > 2.0$ will typically give 36 hits per track. The TRT gives an intrinsic posision resolution of 130 μm in $(R - \phi)$.

4.3.3 The Calorimeters

Figure 4.7 shows an enlarged three-dimensional view of the electromagnetic and hadron calorimeters, that are located around the central solenoid. Both calorimeters are sampling calorimeters and are designed to yield energy measurements with high accuracy.

The Electromagnetic Calorimeter (EM)

The EM calorimeter is a lead-LAr sampling calorimeter, segmented into a barrel and two endcaps. The depth is > 22 (24) radiation lengths (X_0) in the barrel (endcaps). The barrel is divided in two identical half-barrels, separated at $z = 0$ with a gap of 4 mm. The coverage in pseudorapidity is $|\eta| < 1.475$. EM calorimeter endcaps are divided into two coaxial wheels, where the inner (outer) wheels have a pseudorapidity coverage of $2.5 < |\eta| < 3.2$ ($1.375 < |\eta| < 2.5$). The geometry provides the EM calorimeter with a complete ϕ symmetry without azimuthal cracks.

The Hadronic Calorimeter

The hadronic calorimeter is located on the outside of the EM calorimeter. It consists of three sub-systems, the tile barrel, LAr hadron end cap calorimeter, and the LAr the forward calorimeter.

The Tile Calorimeter consists of steel as the absorber and uses scintillating tiles as the active material. It is arrange into a barrel, and two extended barrels. The barrel (extended barrels) are 5.8 m (2.6 m) long, and have an inner (outer) radius of 2.28 m (4.25 m). The tile calorimeter has a radial depth of approximately 7.4λ (interaction lengths). Each of the barrels consists of 64 modules, where each of the modules is covering 5.625 degrees in azimuth angle. The barrel covers the pseudorapidity of $|\eta| < 1.0$ and the two extended barrels cover $0.8 < |\eta| < 1.7$.

The LAr hadronic end-cap calorimeters consist of two independent wheels per end cap. Covering the range $1.5 < |\eta| < 3.2$, it slightly overlaps the forward calorimeter. Each end cap consists of 32 identical wedge-shaped modules. Closest to the IP it is built up by 25 mm thick copper plates, with spacing of 8.5 mm filed with LAr. Further away from the IP the copper plates size changes to 50 mm.

The LAr forward calorimeters consist of three modules in each end cap, it covers the pseudorapidity range $3.1 < |\eta| < 4.9$. Covering the high η region, it is exposed to high particle fluxes, therefor the LAr gaps are reduced to >2 mm. The first module, consists of copper, and is built for electromagnetic measurements, while the last two modules are made of tungsten, and are designed to predominantly measure hadron interactions. The LAr forward calorimeter is approximately 10λ deep.
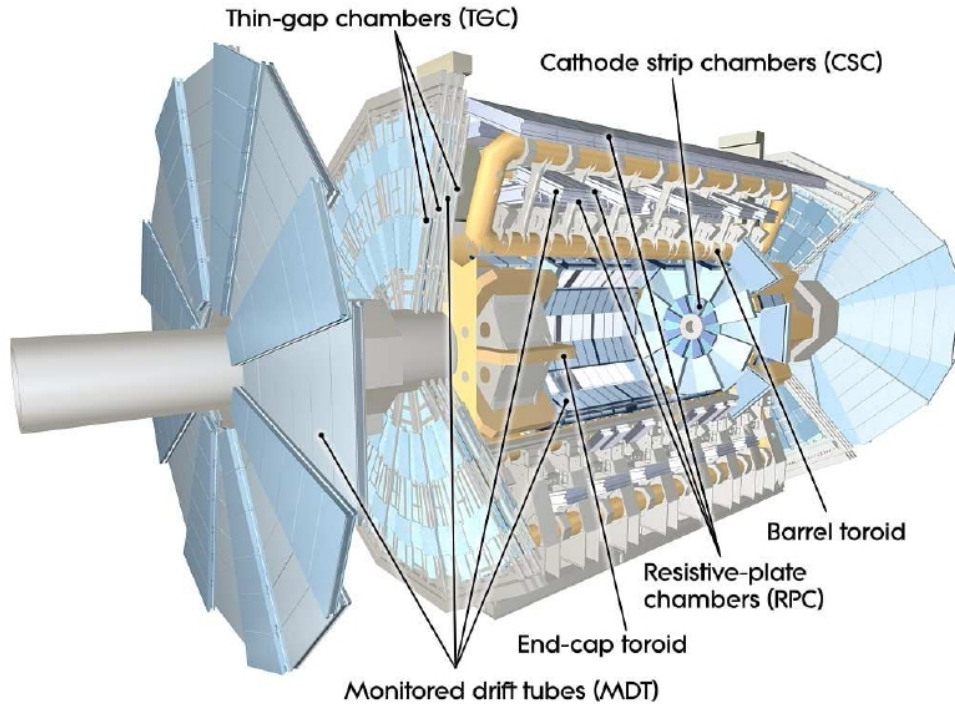
Figure 4.8: Overview of ATLAS muon system, indicating where the different detector are located.

4.3.4   The Muon Spectrometer

Figure 4.8 shows the ATLAS muon spectrometer, which is the largest sub system in the ATLAS detector. It is designed to detect muons and measure their momentum in the range $|\eta| < 2.7$. The muon spectrometer uses magnetic deflection in order to bend the charged particles track in (R-z) direction, thus making momentum measurement possible. To do so, it uses a large superconducting air-core toroid magnet. Four different systems are used to provide precision tracking and a fast trigger system. The tracking is done by the Monitored Drift Tubes (MDTs) and Cathode-Strip Chambers (CSC), while the trigger system consists of the Resistive Plate Chambers (RPC) and Thin Gap Chambers (TGC)

The Monitored Drift Tubes cover most of the pseudorapidity range. They consist of three to eight layers of drift tubes, covering $|\eta| < 2.7$ (except for the innermost end-cap layer, where $|\eta| < 2.0$). The MDT give an average spatial resolution of 80 μm per tube, and about 35 μm per chamber (in z).

The Cathode-Strip Chambers are multiwire proportional chambers, and is used in the forward region ($2.0 < |\eta| < 2.7$). The CSCs have a high rate capability and time resolution

of about 7 ns. Providing both R and ϕ measurement, the CSCs have a position resolution of 40 μm in R and 5 mm in ϕ.

The Resistive Plate Chambers are gaseous parallel electrode-plate detectors, which cover $|\eta| < 1.05$. The RPC have a spatial resolution of 10 mm (z) and 10 mm (ϕ), and a time resolution of 1.5 ns.

The Thin Gap Chambers are multi-wire proportional chambers. They covers the pseudorapidity range of $1.05 < |\eta| < 2.4$. They have a spatial resolution of 2-6 mm (R) and 3-7 mm (ϕ), while the time resolution is 4 ns.
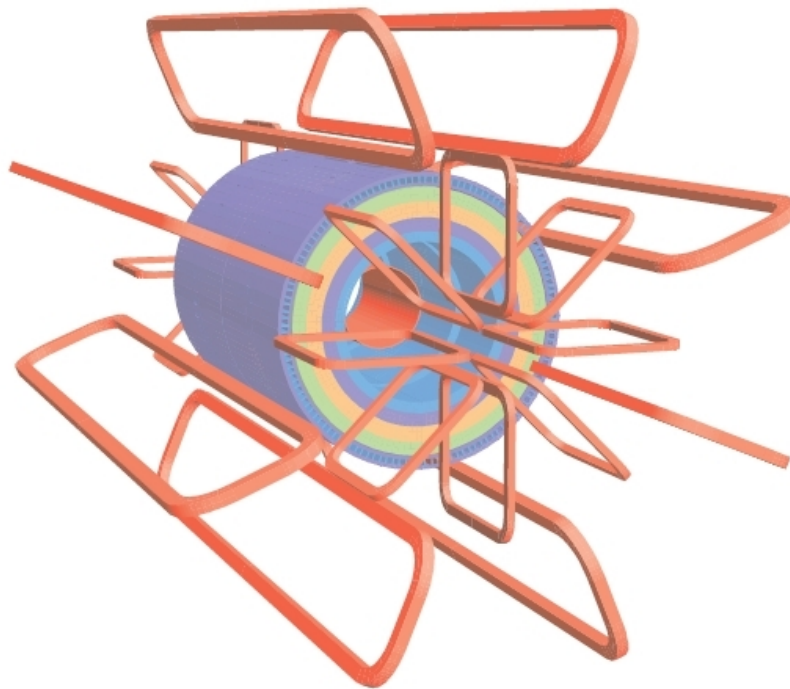
4.3.5 The Magnet System

Figure 4.9: Overview of the geometry for the ATLAS magnetic system. The eight coils in the barrel and the end-cap are visible, located around the tile calorimeter steel. The solenoid windings are located inside the calorimeter volume.

The magnetic system of the ATLAS detector consists of the central solenoid and the air-core toroids. Figure 4.9 shows the geometry of the magnets. Together they will provide the ATLAS detector with the necessary magnetic field to bend charge track, thus making

momentum measurements possible.

The Central Solenoid is located around the Inner Detector. Providing a magnetic solenoidal field to the inner detector with a magnetic field strength of 2 T. Thus, charged track are deflected in the transverse plane, providing p_T measurement. The inner (outer) diameter of the solenoid is 2.46 m (2.56 m). The total length of the central solenoid is 5.8 m.

The air-core toroids are segmented into a barrel and two end caps. They are designed to deflect muons in the (R-z) plane. Each of the three toroids consists of eight coils, placed symmetrically around the beam axis. The central toroid provides a magnetic field of 0.5 T, while the end cap provide a magnetic field of 1.0 T. The barrel has a length of 25.3 m, and has a inner (outer) diameter of 9.4 m (20.1 m).

4.3.6 The Trigger System

The design luminosity of 10^{34}cm^{-2}s-1 will correspond to approximately a interaction rate of 1 GHz. This is a huge amount of data, that needs to be reduced to a rate of 200 events per second. The trigger consists of three levels of online event selection, the Level-1 Trigger, Level-2 Trigger and Event Filter. The Level-2 Trigger and the Event Filter together make up the High-Level Trigger. Figure 4.10 gives an short overview of the ATLAS trigger system, indicating the rate, and latency for each trigger level.

The Level-1 Trigger is based on the information provided by a subset of the detectors. It searches for signatures from high P_T muons, photons, electrons, jets and tau decaying to hadrons. It also searches for large missing energy and large total transverse energy. For the muon momentum search it uses the muon trigger system. It also uses information of all the calorimeters, for identify electromagnetic clusters, jets, τ-leptons, E_T^{miss} and total transverse energy. Events that pass the Level 1 Trigger will define a Regions of Interest (RoIs) and the information is sent to the Level 2 trigger. The RoIs is characterized by there coordinates in η and ϕ. The Level-1 Trigger accept rate is 75 kHz, with a design latency 2.5 μs.

The Level-2 Trigger receives the RoIs from the Level-1 Trigger. It uses the full granularity and precision of all the data, including the inner detector, to further reduce the amount of data. It uses the information from the inner detector to confirm track and energy cluster found in the Level-1 trigger. The Level-2 Trigger is designed to reduce the trigger rate to approximately 3.5 kHz, with processing time of 40 ms.

The Event Filter is the last stage in the online selection, and it will decide which events will go to permanent storage. The Event Filter reduces the trigger rate further, to approximately 200 Hz, with a processing time of 4 s. Once an event is selected by the event
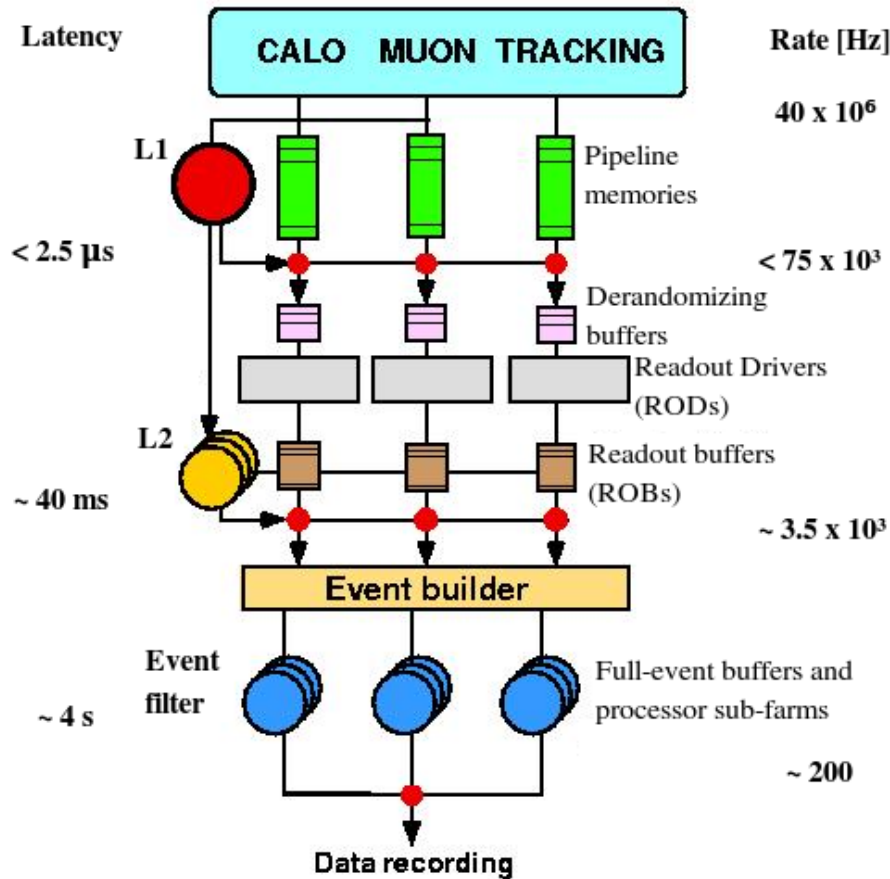
Figure 4.10: Schematic for the ATLAS trigger system, with rate and latency for each level.

filter it will be send to permanent storage, and is available for future physic analysis, the average event size is 1.3 MB.

4.4 Current Performance

ATLAS and the LHC is currently in the start phase of colliding protons whit a center of mass energy of 7 TeV. Data have just recently be started analyzing, Figure 4.11 shows the invariant mass distribution for two opposite charge muons. This plot was made by the ATLAS muon group, and was made by using 320 μb^{-1} of data. The mean value for the gauss curve is at 3.06 ± 0.02 GeV.
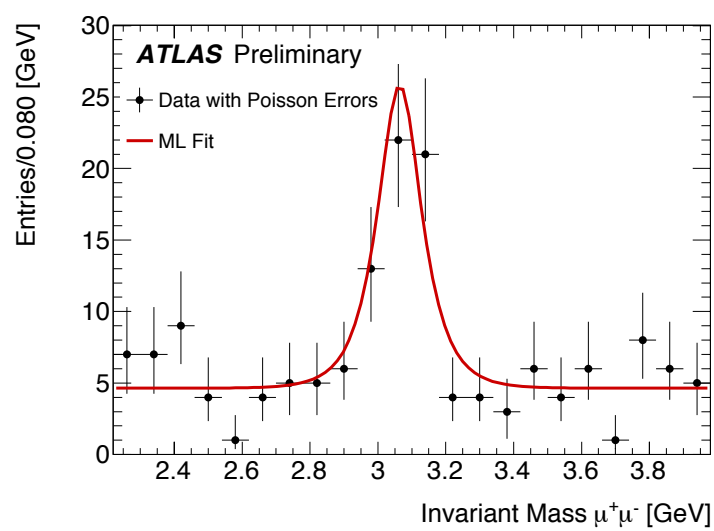
Figure 4.11: Di-muon invariant mass distrubution [23]

Chapter 5

Data Production and Analysis Tools

5.1 Monte Carlo Event Generators

Monte Carlo simulations are an analysis tool to study signatures of specific processes in a detector. This allows development of selection criteria for optimizing the signal to background ratio. Monte Carlo simulations use random sampling as a way simulate a given process. *Event generators* are buildt to simulate hypothetical events taking place in the real detector. In ATLAS, a number of different event generators are used, for a general-purpose MC generators like PHYTHIA, HERWIG, Sherpa, AcerMC, ALPGEN, MadGraph/MadEvent and MC@NLO are used. There are also event generators that are used to simulate specific processes, like Charybdis, BlackMax etc.

- *PYTHIA* is a general purpose event generator [24].

- *HERWIG* is often used to simulate SUSY events [25].

- *Sherpa* is used for simulation of electroweak bosons events, which also include jets [26].

- *AcerMC* is often used for processes that involve heavy quarks, like $Zb\bar{b}$ and $Zt\bar{t}$ [27].

- *ALPGEN* is used for generation of multi-parton processes in hadron collisions, which include electroweak bosons and jets [28].

- *MadGraph/MadEvent* is used for processes where multiple electroweak bosons are simulated, as for example the pair production of ZZ [29].

- *MC@NLO* includes next to leading QCD corrections, and is used to simulate a number of different processes like W or Z production, Higgs production and decay [30].

5.2   Detector Simulation

Specific decay modes are generated by special event generators. In addition a simulation of the detector response is necessary in order to produce simulated samples that are as close to real data as possible. The full simulation, simulat all particles as they move through the ATLAS detector, simulating hits in the different detector elements. Through procedure is not perfect, it counts for most effect. However this is time consuming and does not allow for creation of large data samples. To create large samples with less accurate detector model, Atlfast was developed. The full simulation is accomplished whit the Geant4 program [31], that generates hits and depositing energy in the calorimeters. Figure 5.1 shows the full chain for production of MC events, as done by Geant4. It also show that Atlfast skip some of the steps that Geant4 uses, making Atlfast 4 or 5 orders of magnitude faster than a full simulation [32].
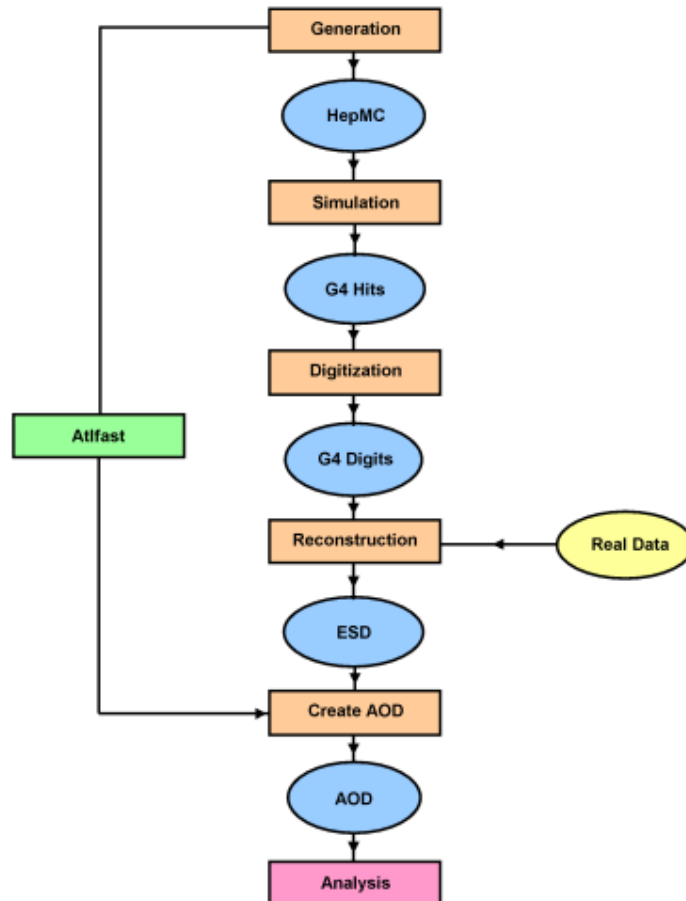

Figure 5.1: The full chain Monte Carlo production [33].

5.3 Charybdis

Charybdis is a Monte Carlo simulation tool, designed to simulate the production and decay of mini black holes, in $p - p$ or in $p - \bar{p}$ collisions. The black hole sample used in this analysis was simulated with Charybdis [34, 35]. Within Charybdis there are several different options for the condition for producing a black hole. The input parameters for the production of the signal sample used in this analysis, are shown in Table 5.1. Grey body factor is a modification to the energy spectrum due to the space-time curvature surrounding the black hole.

Table 5.1: List the input parameter used with Charybdis in creation of the black hole signal sample.

Description	Value
Planck Mass	1 TeV
Total number of dimensions	6
Minimum mass	5 TeV
Maximum mass	10 TeV
Number of particles in remnant decay	2
Beam energy	5 TeV
Time variation of temperature	True
Grey body factors	True
Kinematic cut of	True
Use all Standard Model particles as decay product	True

5.4 BlackMax

BlackMax simulates the production and evolution of mini black-holes and string balls. The BlackMax generator includes options for simulating black holes with gray-body factor. It can simula black-hole rotation, splitting between the fermions, non-zero brane tension and the black hole recoil due to Hawking radiation [36]. The string ball signal was generated by the BlackMax generator, and Tabel 5.2 shows some of the input parameters used in creation of the signal sample.

Table 5.2: List the input parameter used with BlackMax in creation of the string ball signal sample.

Description	Value
Planck Mass M_D	1.3 TeV
String Scale M_S	1 TeV
String coupling g_S	0.4
Number of extra dimensions	6
Minimum mass	3 TeV
Maximum mass	7 TeV
Center of Mass energy	7 TeV

5.5 Data Formats

Several data formats are in use within the ATLAS experiment, each containing different level of information. In this section a short overview is given:

- Raw Data Object (ROD):
  The ROD is a data format used only for Monte Carlo simulations. It is a form of simulated data that closely should reproduce the real bytestream data [37].

- Raw Bytestream Data (RAW):
  The RAW data come from the triggers and online reconstruction. The size of the RAW data is about 1.6 MB per event, and arrives from the Event Filter with a rate of 200 Hz. The RAW data is written to a 2 GB file containing 1250 events [37].

- Event Summary Data (ESD):
  ESD is produced from the RAW data, and is considered as the most basic form of data used for physic analysis. The size of the ESD data is about 500 kB per event [37].

- Analysis Object Data (AOD):
  AOD is produced from the ESD, but are considerable slimmed down in size to about 100 kB per event. The AOD contains data that are necessary for physic analysis [37].

- Derived Physics Data (DPD):
  DPD are slimmed events derived from AOD, on which the end user can perform physics analyses on. They are n-tupel style representations that can be used easily with analysis tools such as ROOT (see section 5.7). The analysis in this thesis has been preformed on DPD with ROOT [37].

5.6 The Athena Framework

Athena is the common software framework for the ATLAS experiment [38]. It is based on the Gaudi framework, which was originally developed by LHCb, but today it is a common kernel of software for both the ATLAS and the LHCb experiments, with Athena including some ATLAS specific program enhancements. All levels of data processing in the ATLAS experiment, are done in the Athena framework [37], that includes software for example for event simulation, event trigger, event reconstruction, and physic analysis tools.

5.7 ROOT

ROOT is a analysis program that is used in all high energy particle physic experiments. It is based on Object Oriented programming, and has a built-in C++ interpreter (CINT). This makes small C++ programs that run, without being compiled. ROOT is designed to handle large amounts of data in a very efficient way. ROOT provides a large amount of analyses tools such as histograms plotting and histogram fitting. ROOT has been used extensively throughout this study, and all plots produced in this study have been done with ROOT.

Chapter 6

Black Hole Reconstruction

We have been studying black hole production and decay in the ATLAS detector. In this study we have used a beam energy of 5 TeV. Our simulated black hole is a non-rotating black hole in 2 extra spatial dimensions, and assumed signal cross section of 3 pb. The signal sample consists of 14750 events, and correspond to a luminosity of ~ 4.9 fb^{-1}. Our goal has been to separate a black hole signal from that of standard model background processes.

6.1 Event selection

Table 6.1: The selection criteria used in the reconstruction of black holes [39].

Selection criteria	
Muon (μ); p$_T$ > 15 GeV $\|\eta\| < 2.5$ track match $0 \leq \chi^2 < 100$ Isolation E$_{T_{cone0.2}} < 0.2$p$_T$+20 GeV	Electron(e); p$_T$ > 15 GeV $\|\eta\| < 2.5$ except $1.00 < \|\eta\| < 1.15$ and $1.37 < \|\eta\| < 1.52$ Electron *Medium* [39]
Photon (γ) p$_T$ > 15 GeV $\|\eta\| < 2.5$ Photon *Tight* [39] Isolation E$_{T_{cone0.2}} < 0.2$p$_T$+20Gev	Jets p$_T$ > 20 GeV $\|\eta\| < 2.5$ Cone4TopoJets

A black hole will decay via Hawking radiation to every type of standard model particles. Thus, we need to reconstruct muons (μ), electrons (e), photons (γ) and jets. Our reconstruction of objects is done in this order. Once an object is chosen, any other object that is within $\Delta R < 0.1$ is removed, where $\Delta R = \sqrt{(\Delta\eta)^2 + (\Delta\phi)^2}$. The fundamental objects we select has to pass certain selection criteria, which are listed in Table 6.1.

A black holes will decay into all standard model particles, including the gauge bosons, W and Z. The W boson will decay to either $W \rightarrow l\nu$, or to hadrons, While the Z boson will decay to $Z \rightarrow ll$, $Z \rightarrow \nu\nu$ or $Z \rightarrow q\bar{q}$. The decay products of W and Z will be reconstructed, and give a contribution to the reconstruction as electrons, muons, jets or $\not{E}_T$.
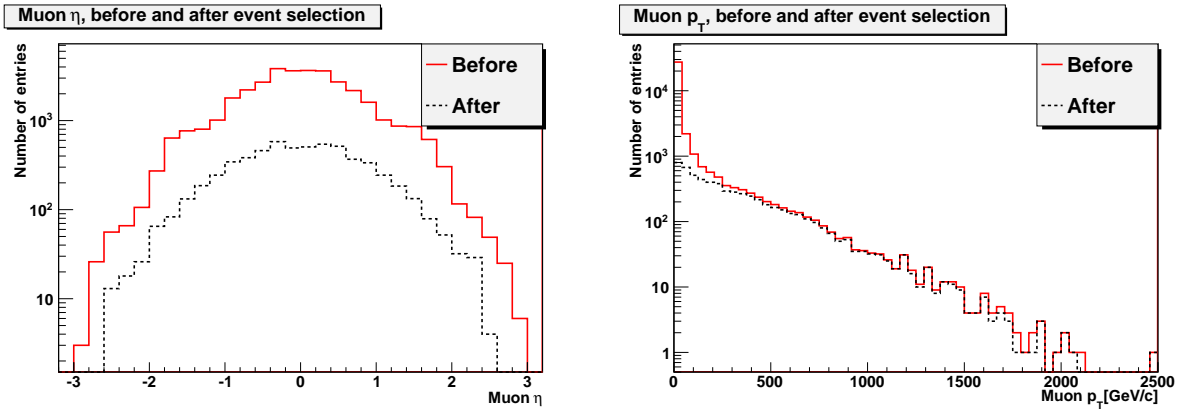
Figure 6.1: The η and p_T distributions of muon tracks, before and after the event selection.
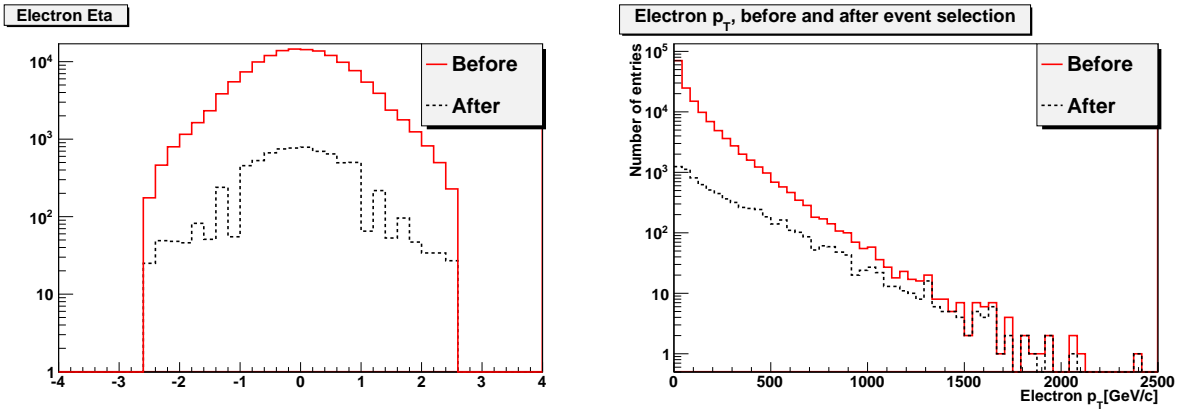
Figure 6.2: The η and p_T distributions of electron tracks, before and after the event selection.
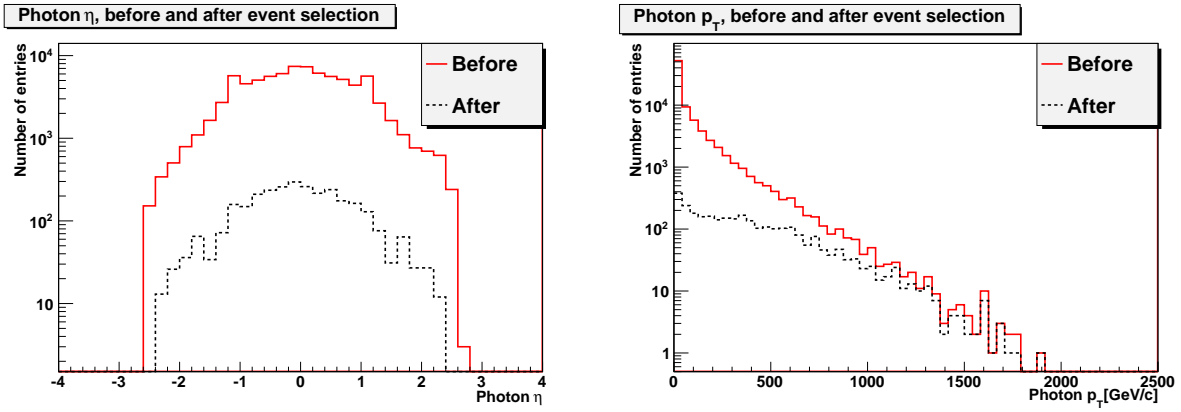
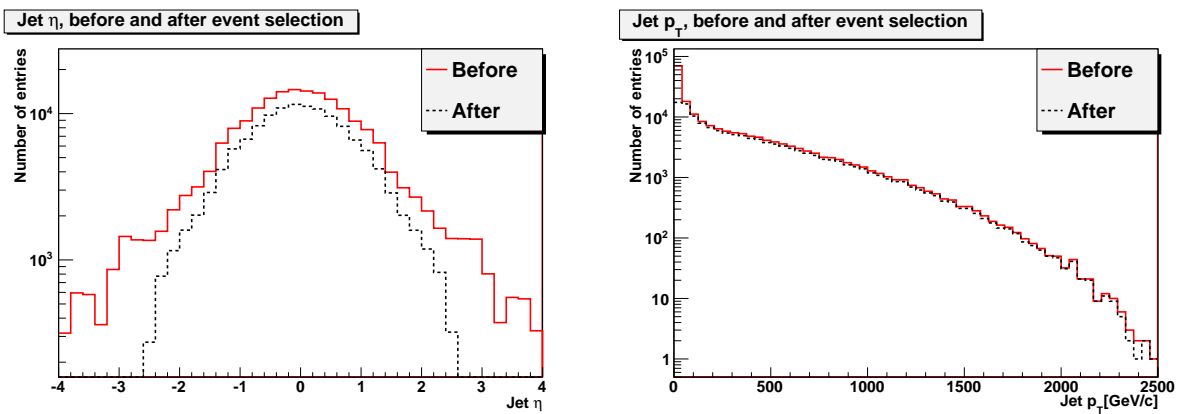*Figure 6.3:* The η and p$_T$ distributions of photon tracks, before and after the event selection.

Figure 6.4: The η and p$_T$ distributions of Jets, before and after the event selection.

6.1.1 Electron and Photon reconstruction

Selection criteria for electrons and photons are dependent on *loose*, *medium* and *tight* cuts. The selection for electrons and photons is done by applying the *IsEM* variable, which is a boolean variable that includes several selection criteria, such as Hadron energy leakage, energy cluster, track matching, and E/p. Using predefine selection criteria is a standard way in the ATLAS experiment to identify photons and electrons. For a full description of these selection criteria, see [39] The *medium* cut for electrons has an expected efficiency of 77.29 ± 0.06 % and a jet rejection factor of 2187 ± 7. The photon reconstruction efficiency for *tight* selection, is for $E_T > 40$ GeV expected to be 86.3 ± 0.2 %.

One of the selection criteria that enters in all of *loose*, *medium* and *tight*, is an observable that is called hadron leakage. Hadron leakage is defined as the ratio of transverse energy deposit in the first layer of the hadron calorimeter, divided by the transverse energy deposited in the electromagnetic calorimeter. Since photons and electrons are electromagnetic showers, they deposit their energy in the electromagnetic calorimeter and not in the hadron calorimeter. Thus, the hadron leakage is an excellent separation of electrons and photons from jets. Figure 6.5 shows the hadron leakage, calculated by using the string ball MC sample discussed in chapter 7. The sample labeled "*Before*" contains all the electron candidates, while the sample label "*After*" removes all the candidates that have not passed the selection criteria from Table 7.1.
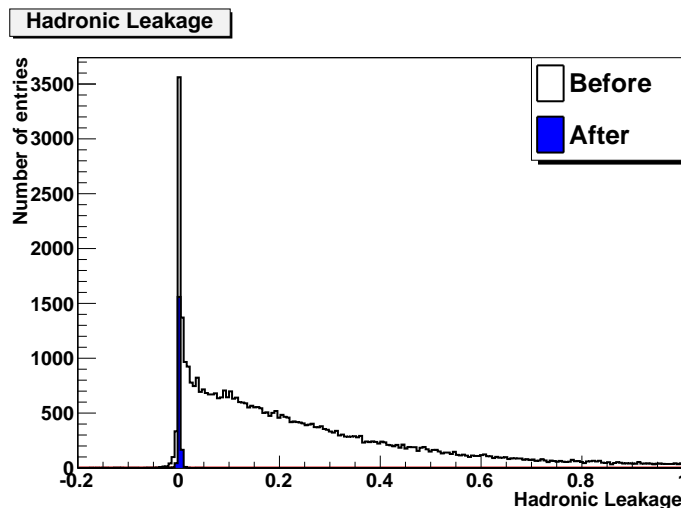

Figure 6.5: Shows the Hadronic Leakage from electrons, calculated from the string ball signal.

6.1.2 Jets

There are several reconstruction algorithms used in the identification of hadronic jets in ATLAS. For this analysis we used the Cone4TopoJets. This cone algorithm collects the topological clusters and tracks in a cone of $\Delta R = \sqrt{\Delta\eta^2 + \Delta\phi^2} < R_{cone}$, where R_{cone} is a fixed cone radius. In Cone4TopoJets a narrow radius of R_{cone}=0.4 is chosen, to determine the four-momentum of the jet.

6.2 Invariant Mass Reconstruction

Our signal sample, consists of 14 750 simulated black hole events. For each event we use all the objects that pass our selection criteria listed in Table 6.1. The black hole mass reconstruction is done by calculating the four-momenta of all reconstructed final state objects (Muons, Electrons, Photons and jets). To improve the mass resolution the missing transverse energy is included in the mass calculation, which distribution is shown in Figure 6.6. Thus, the black hole mass is simply calculated by

$$
\begin{aligned}
m_{BH} &= \sqrt{p_{BH}^2}, \\
p_{BH} &= \sum_i p_i + \left(\not{E}_T, \not{E}_{T_x}, \not{E}_{T_y}, 0 \right),
\end{aligned}
\tag{6.1}
$$

Figure 6.7 shows the resulting invariant mass distribution calculated for all objects that passed the selection criteria listed in Table 6.1, while Figure 6.8 shows the same distribution without the missing energy included in the calculation. Note that the distribution that omits $\not{E}_T$ is peaked at lower mass and is wider.
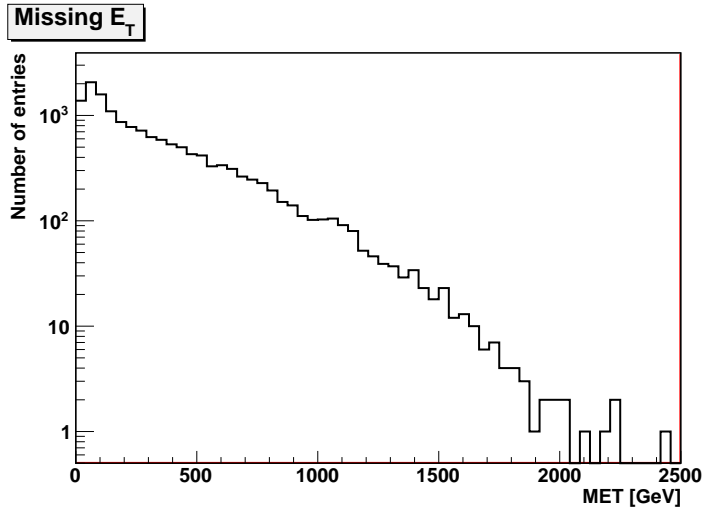

Figure 6.6: Missing energy distribution from signal sample
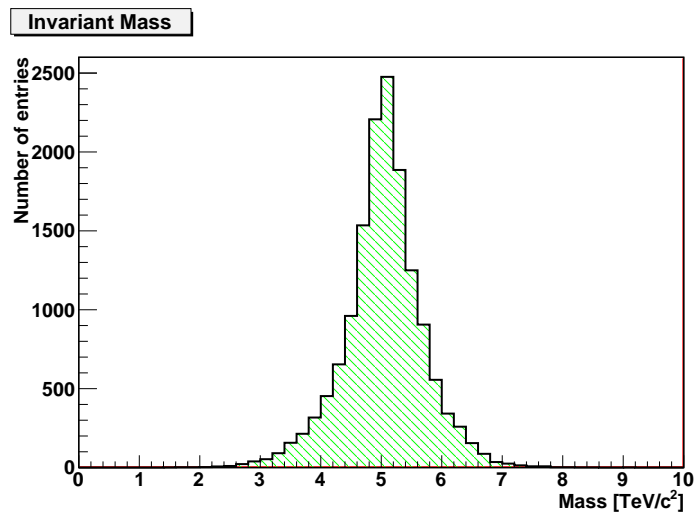
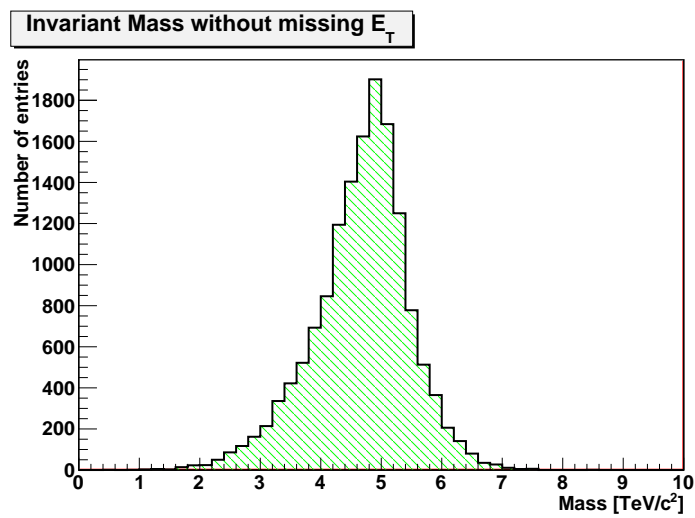*Figure 6.7:* Invariant Mass distribution, calculated by using equation 6.1.

Figure 6.8: Invariant Mass distribution, without including the missing transverse energy in the calculation.

6.2.1   The Background Samples

The relevant background to a back hole signal, will be highly energetic events. Events with high $\sum |p_T|$, and high multiplicity of fundamental objects, are of interest. The main background that we have studied is $t\bar{t}$ production, dijet production, $W \rightarrow l\nu$+jets production, and $Z \rightarrow ll$+jets production.

Dijet production is one of the most common processes in particle physics experiments. Since dijet have a large production cross section, they provides a considerable source of background for many rare processes. To the lowest order it is a $2 \rightarrow 2$ scattering process between two partons, resulting in the production of hadronic jets. In ATLAS MC dijet samples are often called JN (where N is 1,2...8), and indicate the momentum range for the leading jets. Since the multiplicity of a black hole depends on the number of extra dimensions, dijet contribution need to be considered. With increasing n, the multiplicity of the decay product is decreasing, making the decay more like a jet-jet like event, as shown in Figure 3.1.
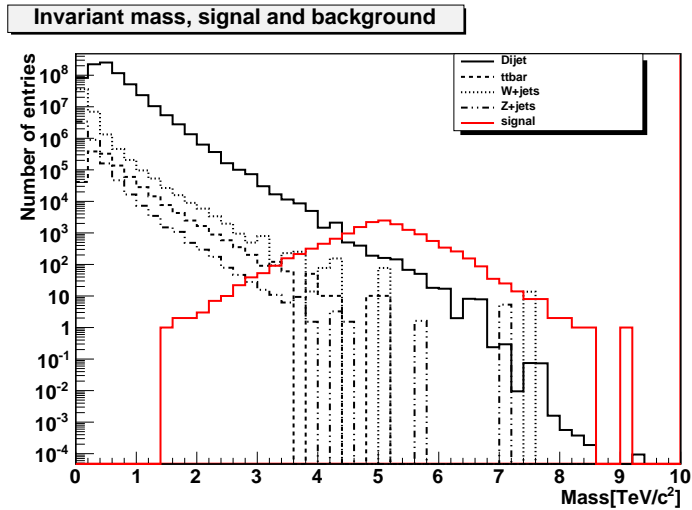

Figure 6.9: Invariant mass distribution, with background without cut

6.2.2   Normalizing the signal and background samples

In order to option the right ratio between signal and background, we have to normalize the signal and background. In this study we normalized the background to the signal, by

scaling the background to the same luminosity as that corresponding to the signal. These weights are given by

$$w = a \frac{\int \text{initial signal histogram}}{\int \text{initial background histogram}} , \qquad (6.2)$$

where w is the weight (listed in Table 6.2), and a is the normalization factor based on the cross section for the separate processes ($\sigma_{backgroun}/\sigma_{signal}$).

Figure 6.9 shows the invariant mass distributions for signal and various backgrounds. The dijet background clearly provides the largest contribution to the background, before any selection criteria is applied. In the lower mass region the background is dominating, but at around 4.2 TeV the signal is also larger then the dijet background.

Figure 6.10 shows the $\sum |p_T|$ distribution from all the objects that pass the selection criteria listed in Table 6.1. We find that the signal becomes larger than the background at about 2.8 TeV. Figure 6.11 shows the number of objects (N), that pass the selection criteria from table 6.1.
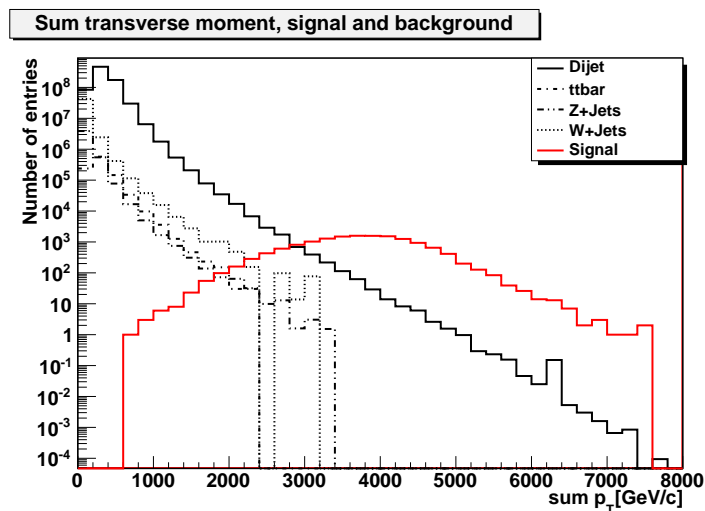

Figure 6.10: $\sum |p_T|$ of all the fundamental object, plotted for the signal and background.
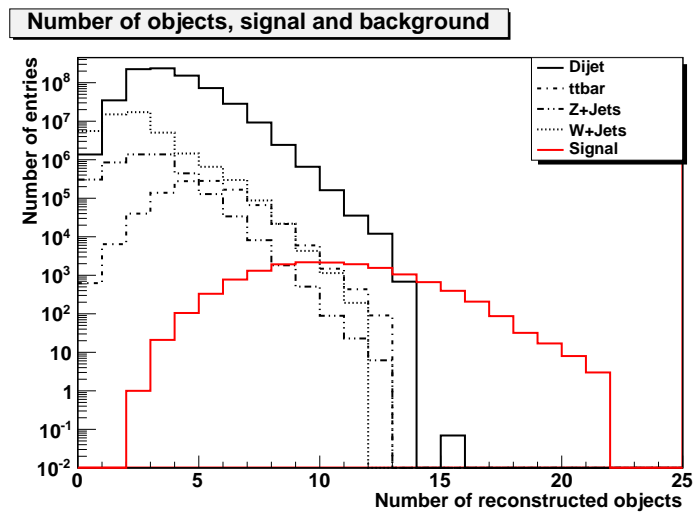
Figure 6.11: Number of reconstructed objects .

Table 6.2: Different background samples that are included in this study. The different dijet sets have their own p$_T$ range for the momentum of the leading jets, J4 has (140 GeV < p_T < 280 GeV), J5 have (280 GeV < p_T < 560 GeV), J6 has (560 GeV < p_T < 1120 GeV), J7 has (1120 GeV < p_T < 2240 GeV), J8 has (p_T > 2240 GeV).

Background Samples				
type	name	cross section (pb)	Number of events	scale factor w
ttbar	$t\bar{t}$	2.05×10^2	99 947	10.085
Dijet	J4	1.5×10^5	71 649	10258
Dijet	J5	5.122×10^3	77 043	325.76
Dijet	J6	1.119×10^2	75 952	7.22
Dijet	J7	1.075	76 312	0.069
Dijet	J8	1.112×10^{-3}	58 120	0.0000938
$W \to e\nu_e$	$W_{e\nu} + 1$ jet	2112.30	200 977	51.5
$W \to e\nu_e$	$W_{e\nu} + 2$ jets	676.00	19 952	166.0
$W \to e\nu_e$	$W_{e\nu} + 3$ jets	203.30	13 992	71.1
$W \to e\nu_e$	$W_{e\nu} + 4$ jets	56.10	20 000	13.7
$W \to e\nu_e$	$W_{e\nu} + 5$ jets	16.60	13 992	5.8
$W \to \mu\nu_\mu$	$W_{\mu\nu} + 1$ jet	2155.50	19 957	529.2
$W \to \mu\nu_\mu$	$W_{\mu\nu} + 2$ jets	682.30	19 958	167.5
$W \to \mu\nu_\mu$	$W_{\mu\nu} + 3$ jets	202.00	19 972	49.6
$W \to \mu\nu_\mu$	$W_{\mu\nu} + 4$ jets	55.50	19 973	13.6
$W \to \mu\nu_\mu$	$W_{\mu\nu} + 5$ jets	16.30	12 975	6.16
$W \to \tau\nu_\tau$	$W_{\tau\nu} + 1$ jet	2106.90	19 000	543.4
$W \to \tau\nu_\tau$	$W_{\tau\nu} + 2$ jets	672.80	19 884	105.8
$W \to \tau\nu_\tau$	$W_{\tau\nu} + 3$ jets	202.70	19 457	51.0
$W \to \tau\nu_\tau$	$W_{\tau\nu} + 4$ jets	55.30	19 815	13.7
$W \to \tau\nu_\tau$	$W_{\tau\nu} + 5$ jets	17.00	12 913	6.45
$Z \to ee$	$Z_{ee} + 1$ jet	206.60	19 861	50.8
$Z \to ee$	$Z_{ee} + 2$ jets	72.50	19 921	17.8
$Z \to ee$	$Z_{ee} + 3$ jets	21.10	19 916	5.2
$Z \to ee$	$Z_{ee} + 4$ jets	6.00	18 470	1.6
$Z \to ee$	$Z_{ee} + 5$ jets	1.70	5 500	1.5
$Z \to \mu\mu$	$Z_{\mu\mu} + 1$ jet	205.20	19 987	50.3
$Z \to \mu\mu$	$Z_{\mu\mu} + 2$ jets	69.40	19 262	17.7
$Z \to \mu\mu$	$Z_{\mu\mu} + 3$ jets	21.60	19 987	5.3
$Z \to \mu\mu$	$Z_{\mu\mu} + 4$ jets	6.10	18 440	1.6
$Z \to \mu\mu$	$Z_{\mu\mu} + 5$ jets	1.70	5 471	1.5
$Z \to \tau\tau$	$Z_{\tau\tau} + 1$ jet	209.30	19 928	50.8
$Z \to \tau\tau$	$Z_{\tau\tau} + 2$ jets	70.20	19 378	17.8
$Z \to \tau\tau$	$Z_{\tau\tau} + 3$ jets	21.10	19 457	5.2
$Z \to \tau\tau$	$Z_{\tau\tau} + 4$ jets	6.00	18 500	1.6
$Z \to \tau\tau$	$Z_{\tau\tau} + 5$ jets	1.70	5 479	1.5

6.2.3 Selection criteria

We optimize the signal yield using the significance,

$$R = \frac{S}{\sqrt{S+B}} \, , \tag{6.3}$$

where S is the number of signal events and B is the number of background events. Because of the high mass and an isotropic decay to a large number of final state objects, a 5 TeV black hole will decay so that each object has a high p_T. Three independent selection criteria were used for this selection, the $\sum |p_T|$, p_T of the 4th leading object, and p_T of the 5th leading object. No other requirements apart from the selection of e, μ, γ and jets, as given in Table 6.1, are imposed. The significance plots are made for a luminosity of 1 fb^{-1}

The optimization with R is done for each observable separately. Figure 6.12 shows R as a function of $\sum |p_T| \geq \sum |p_T|_{min}$, where $\sum |p_T|_{min}$ is the minimum requirement on the summed transverse momentum. The range starts form 2 TeV/c and ends at 4.2 TeV/c, separated into interval of 200 GeV/c. The highest significance is achieved at approximately ~ 2.8 TeV/c.
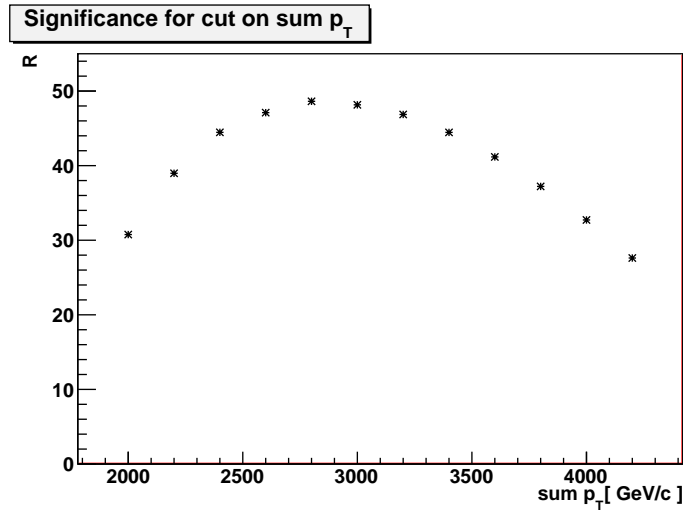

Figure 6.12: Sensitivity for $\sum |p_T|$ cut, for 1 fb^{-1} of data.

Figure 6.13 shows the significance for a minimum requirement on the p_T of the 4th leading object. We studied the range from 40 GeV/c to 400 GeV/c, in steps of 40 GeV/c. The highest significance is found for $p_T \geq 330$ GeV/c. Figure 6.14 shows the significance for a
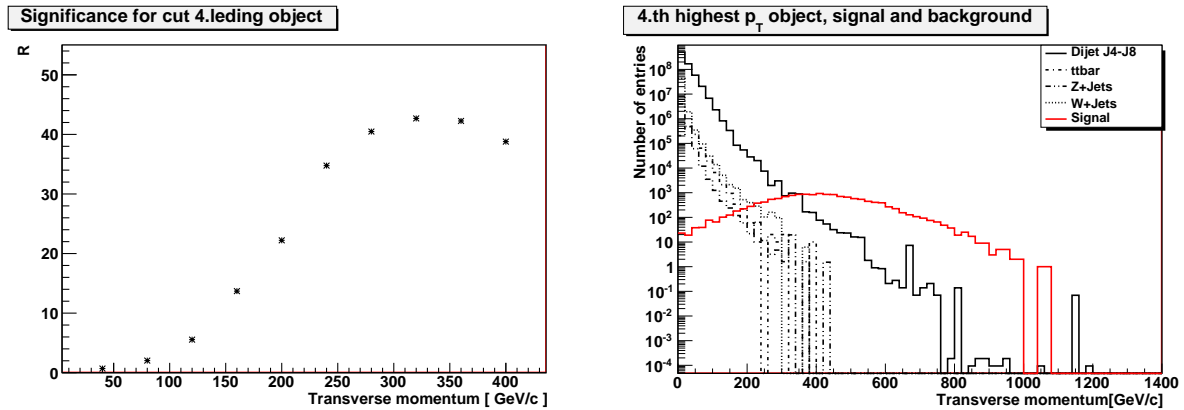
minimum requirement on the p$_T$ of the 5h leading object. We studied the range from 40 GeV/c to 400 GeV/c, in steps of 40 GeV/c. The highest significance is found for p$_T \geq$ 200 GeV/c.
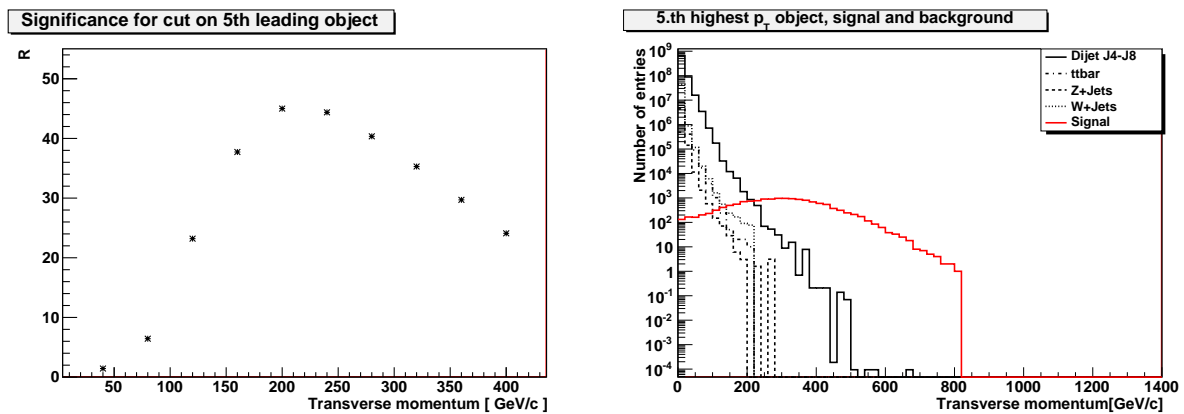

Figure 6.13: (Left:) significance as a function on the minimum transverse momentum of the 4th highest momentum object, for 1 fb^{-1} of data. (*Right:*) p$_T$ distribution for signal and background for the 4th highest transverse momentum object.

Figure 6.14: (Left:) significance as a function on the minimum transverse momentum of the 5th highest momentum object, for 1 fb^{-1} of data. (*Right:*) p$_T$ distribution for signal and background for the 5th highest transverse momentum object.

In order to get a better understanding of the background and signal, we made some scatter plots for the black hole versus the variable we optimize the signal yield on. In Figure 6.15 we have plotted the $\sum |p_T|$ vs the mass, for the signal, and for the J4 and J7 dijet backgrounds. The J4 background has low $\sum |p_T|$ compared to the signal, while the J7 will have a larger number of events that pass a $\sum |p_T| > 2.8$ TeV requirement. The horizontal line shows the optimum selection requirement.
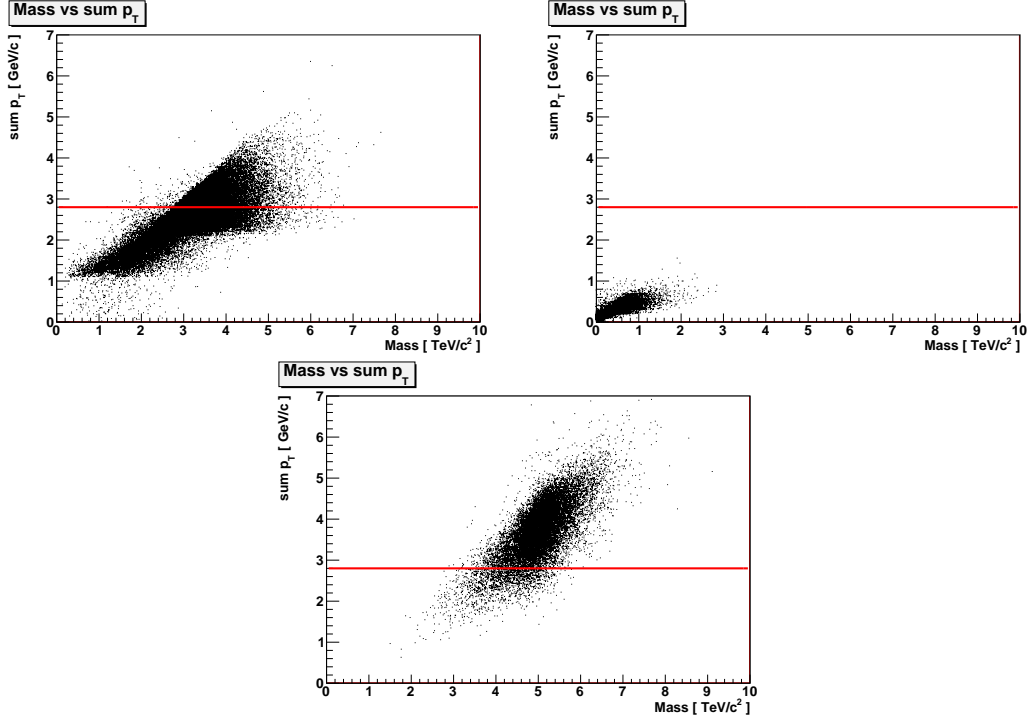
Figure 6.15: (*Upper left:*) shows the black hole invariant mass vs $\sum |p_T|$ for the J7 background. (*Upper right:*) shows the black hole invariant mass vs $\sum |p_T|$ for the J4 background. (*Lower center:*) shows the black hole invariant mass vs $\sum |p_T|$ for the black hole signal.

In Figure 6.16 the p_T of the 4th leading object vs the mass was plotted. J4 will give a little contribution to the signal region, while J7 have a great number of events that will pass a requirement on the 4th leading object, $p_T > 330$ GeV/c.
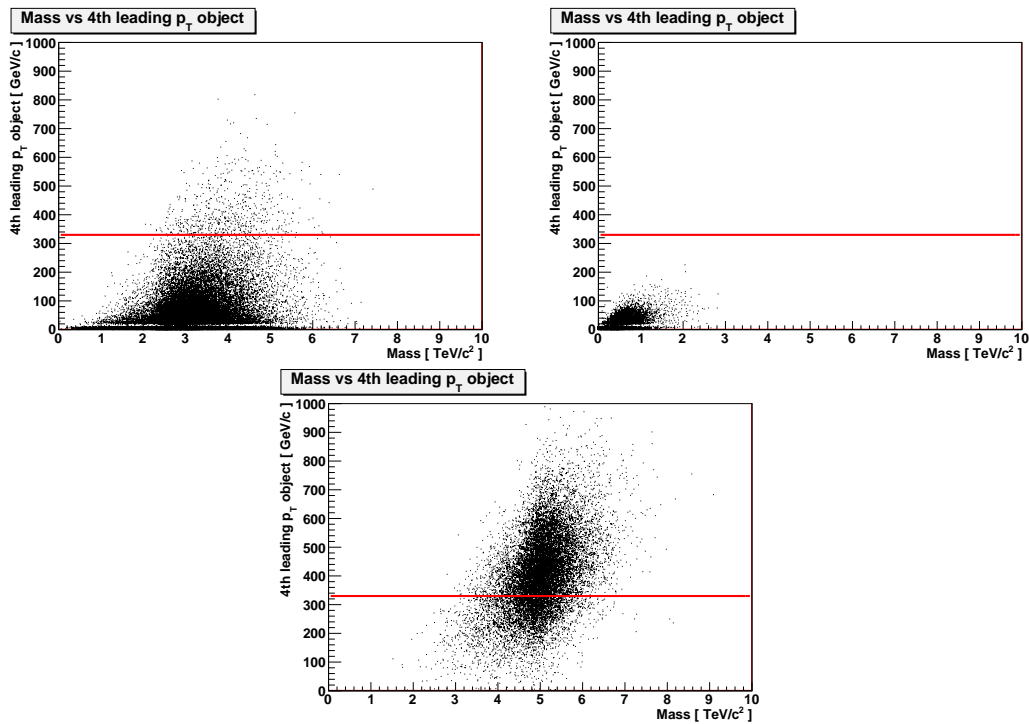
Figure 6.16: (*Upper left:*) shows the black hole invariant mass vs p_T for the 4th leading object, for the J7 background. (*Upper right:*) shows the black hole invariant mass vs p_T for the 4th leading object, for the J4 background. (*Lower center:*) shows the mass black hole invariant vs p_T for the 4th leading object, for the black hole signal.

Figure 6.17 shows the p_T of the 5th leading object vs the mass. The J4 background can be neglected if a $p_T > 200$ GeV/c is required on the 5th leading object. From the J7 distribution we find that not many J7 events will pass a requirement on the 5th leading objet $p_T > 200$ GeV/c, while most of the signal passes this requirement. A requirement on the p_T for the 5th leading object will have more affect on the J7 background, compared to that of a $\sum |p_T|$ requirement.
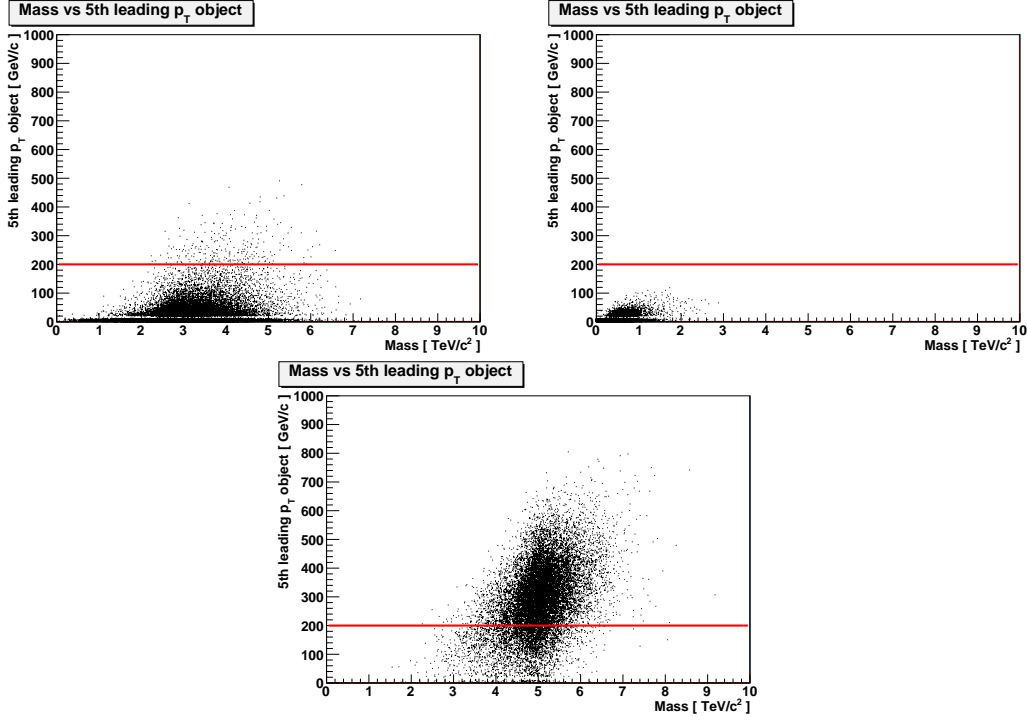

Figure 6.17: (Upper left:) shows the black hole invariant mass vs p_T for the 5th leading object, for the J7 background. (*Upper right:*) shows the black hole invariant mass vs p_T for the 5th leading object, for the J4 background. (*Lower center:*) shows the black hole invariant mass vs p_T for the 5th leading object, for the black hole signal.

6.2.4   Invariant Mass Reconstruction after optimization

Applying the selection criteria from Table 6.1, and requiring that $\sum |p_T| > 2.8$ TeV/c, we reconstruct the invariant mass for the black hole. Figure 6.18 shows the invariant mass distribution for a black hole. Note that the $t\bar{t}$ background has been completely removed, and only a few events of W and Z background remain. The dijet background is quite small, but large compared to the W and Z backgrounds. Table 6.3 shows the number of events that survive the $\sum |p_T| > 2.8$ TeV/c requirement. The background is normalized to the signal.

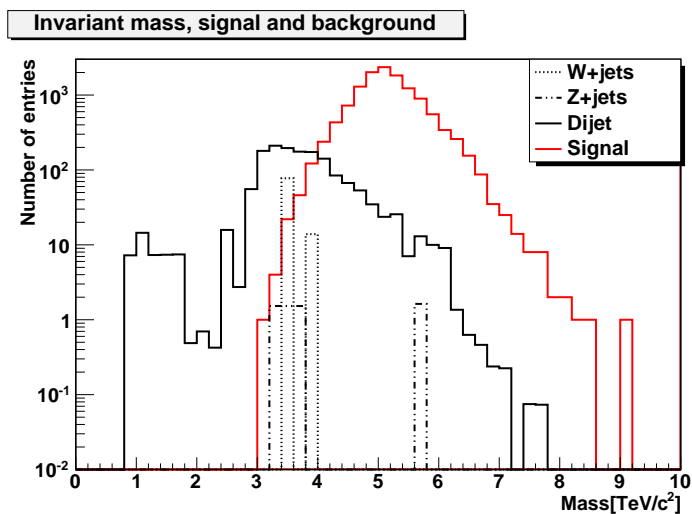*Figure 6.18:* Invariant mass distribution after requirement $\sum |p_T| > 2.8$ TeV

Table 6.3: Black Hole selection reconstruction efficiencies, after applying the selection criteria in Table 6.1 and requiring $\sum |p_T| > 2.8$ TeV/c. The final number of events are rounded off to the closest integer number.

Black Hole reconstruction efficiency			
Signal	Efficiency	Initial number of events	Number of events after require $\sum |p_T| > 2.8$
Black Hole Signal	86.1%	14750	12714
Dijet		$7.7 \cdot 10^8$	1527 ± 54
W+jets		$4.5 \cdot 10^7$	91 ± 72
Z+jets		$4.5 \cdot 10^6$	6 ± 3
$t\bar{t}$		$1.0 \cdot 10^6$	0

Figure 6.19 show the invariant mass after requiring that the $\sum |p_T| > 2.8$ TeV/c and the 5.th leading object has $p_T > 200$ GeV/c. Here the W background is also completely removed, while Z and the dijet backgrounds are also reduced compared to Figure 6.18. Table 6.4 shows the number of events that survive a requirement on the $\sum |p_T| > 2.8$ TeV/c and the $p_T > 200$ for the 5th leading object. The background is normalized to the signal.
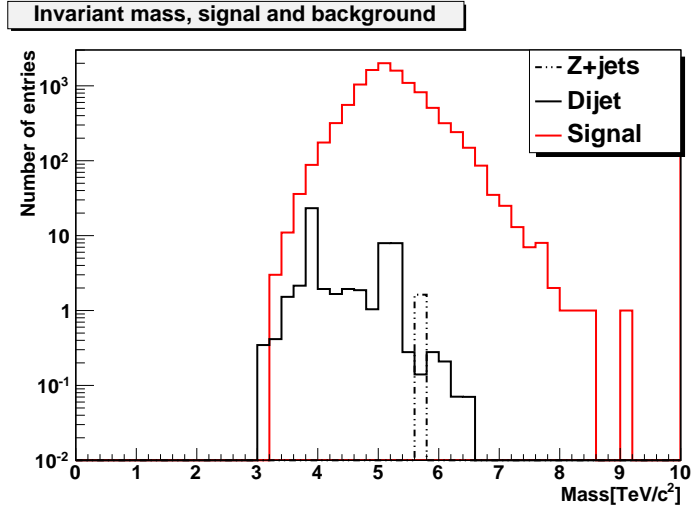

Figure 6.19: Invariant mass distribution after requiring that $\sum |p_T| > 2.8$ TeV and that the 5.th leading object has $p_T > 200$ GeV.

Table 6.4: Black Hole selection efficiencies, after applying the selection criteria from Table 6.1 and requiring $\sum |p_T| > 2.8$ TeV/c, and the $p_T > 200$ GeV/c for the 5.th leading object. The final number of events is rounded off to the closest integer number.

Black Hole reconstruction efficiency			
Signal	Efficienscy	Initial number of events	Number of events after require $\sum |p_T| > 2.8$ and the 5.th leading object has $p_T > 200$ GeV/c
Black Hole Signal	73.0%	14750	10765
Dijet		$7.7 \cdot 10^8$	53±16
W+jets		$4.5 \cdot 10^7$	0
Z+jets		$4.5 \cdot 10^6$	2±2
$t\bar{t}$		$1.0 \cdot 10^6$	0

Although the LHC is not going to be colliding protons at a center of mass energy of 10 TeV, this was a previously planed to be the start up energy. This is the reason why this study was preformed, at this energy. We wanted to look at the discovery potential for black hole production, at this energy. Figure 6.20 shows the significance plotted as a function of luminosity, when we require $\sum |p_T| > 2.8$ TeV/c, and $p_T > 200$ GeV/c for the 5th leading object. The horizontal line shows where the significance $(S/\sqrt{S+B})$ gives a 5σ value. This is achieved for an luminosity of ~ 12 pb^{-1}. Figure 6.21 shows the significance R, plotted
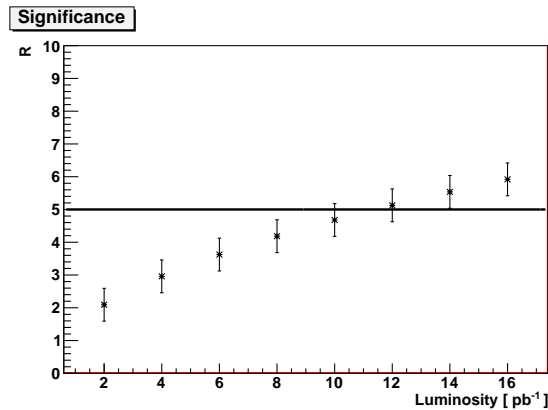

Figure 6.20: Significance R, plotted as a function of luminosity.

as a function of cross section, when we require $\sum |p_T| > 2.8$ TeV/c, and the $p_T > 200$ GeV/c for the 5th leading object. Here we assume an integrated luminosity of 1 fb^{-1}. The horizontal line is plotted at 5σ. A 5σ discovery is possible, if the black holes cross section is larger than ~ 0.023 pb. If ATLAS was operating at a center of mass energy of 10 TeV,
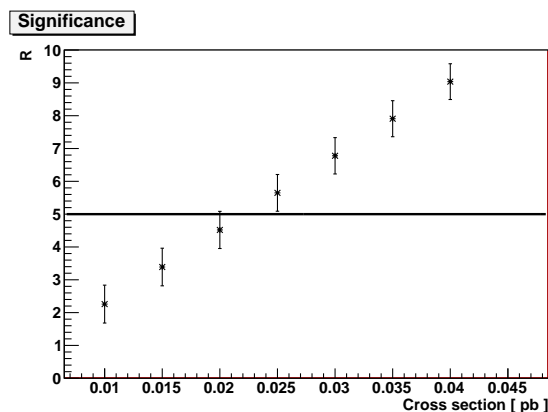

Figure 6.21: Significance R, plotted as a function of cross section.

and no black hole events were found in the first 1 fb^{-1} of data, limits could be set on the cross section by using the Bayesian approach [3], and taking our reconstruction efficiency

in to account (from Table 6.4). Assuming a Poisson distribution, and zero observed event, the 90% upper limit can be calculated by

$$\frac{\nu_{up}}{\epsilon \cdot \mathscr{L}} = \frac{2.30}{0.73 \cdot 1 fb^{-1}} = 3.15 fb. \tag{6.4}$$

If no observed black holes are found in the first 1 fb^{-1} of data, 90% upper limit (95%) can be set at $\sigma_{BH} < 3.15$ fb (4.11 fb).

6.2.5 Errors

There are factors that will affect the discovery of black holes, that have not been taken in to account in this study. A statistical error will affect the background distributions, due to the fact that these distributions get scaled. Each background sample will get its own scaling factor w (see Table 6.2), due to the different cross section, and the number of events in the MC samples. In the worst case, one event can get scaled with a factor of 10258. Although, after the final selection criteria, the background is dominated by the J6, J7, J8 backgrounds, and here the scaling factors are small, and J7 and J8 will get down scaled. This error may effect our optimization.

There is also an error in the cross section for the background. The cross sections for the different background samples are calculated from known processes at lower energies, and then they are extrapolated to higher energies. Thus, there is a systematic error from this. However in the final selection the background contribution is small, and hence the impact of this error is small.

The reconstruction of black holes (and string balls, see Chapter 7) will also be affected by the ATLAS trigger. But since the decay of black hole include multiple high p$_T$ jets. The efficiencies for trigger on a black hole event is expected greater then 99% [40].

There is also be an error in our selection procedure, which are not taken in to account. The same errors will also effect the string ball reconstruction in Chapter 7.

Chapter 7

String Balls

In the first period of data taking (1 fb^{-1}), the LHC is operating with a center of mass energy at 7 TeV. At this energy, black hole production is rather unlikely, but highly exited string states may be produced. In the light of this we have performed a study to detect string ball. In this chapter, all plots are normalized to an integrated luminosity of 1 fb^{-1}.

7.1 Signal

The string ball signal sample used in this section contains 4966 simulated Monte Carlo events. The sample is simulated with a mass of 3 TeV/c^2 in 6 spatial dimensions. The String scale was set to $M_S = 1.0$ TeV/c^2, while the Planck mass was set to $M_D = 1.3$ TeV/c^2. The cross section used for the signal is 2 pb [41]. The decay of a string ball is expected to have many of the same characteristics as the decay of a black hole. So reconstruction of string balls have many of the same observables as those for black hole reconstruction. We select muons, electrons, photons and jets in this order. Once an object is selected, any other object that passes within a cone of radius $\Delta R < 0.1$ is removed.

7.2 Invariant Mass

To calculate the invariant mass of a string ball, one uses all objects that pass the selection criteria listed in table 7.1. For selected objects the invariant mass of a string ball is then calculated using Equation 6.1. Figure 7.1 shows the invariant mass distribution from string balls with background without any requirements on the selection criteria other then those

Table 7.1: The selection criteria used in the reconstruction of string balls.

Selection criteria	
Muon (μ);	Electron(e);
$p_T > 15$ GeV/c	$p_T > 15$ GeV/c
$|\eta| < 2.5$	$|\eta| < 2.5$ except
track mach $\chi^2 < 100$	$1.00 < |\eta| < 1.15$ and $1.37 < |\eta| < 1.52$
Isolation $E_{T_{cone0.2}} < 0.2p_T + 20$ GeV	Electron *Medium*
Photon (γ)	Jets
$p_T > 15$ GeV/c	$p_T > 20$ GeV/c
$|\eta| < 2.5$	$|\eta| < 5$
Photon *Tight*	Cone4TopoJets

Figure 7.1: Invariant mass distribution string ball signal and background, with no cuts applied.

listed in Table 7.1. At 3 TeV/c^2 the signal is 3 orders of magnitude smaller than the background. At higher mass values the S/B is $< 10^{-2}$, and at lower masses this ratio is considerable smaller. As shown later, the background can be suppressed. Figure 7.2 shows the transverse missing energy that is included in the calculation for the invariant mass. Table 7.2 shows the background sample in this analysis, which consists of different dijet samples[1]. The $t\bar{t}$, W plus jets and Z plus jets are omitted, since these backgrounds were found to be negligible in the black hole analysis.

---

[1] If it exist, higher transverse momentum dijet set should be included. But for 7 TeV collisions we have not been able to locate it.
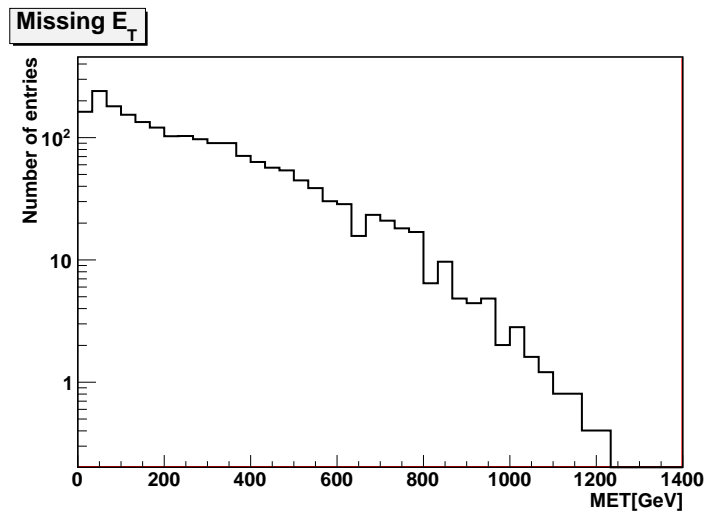
Figure 7.2: Missing transverse energy from the string ball signal.

Table 7.2: List of 7 TeV background samples used as backgrounds in the string ball study. For each background sample the range in p_T is listed.

Background Samples			
type	name	cross section (pb)	Number of events
Dijet	J3(70 GeV/c < p_T < 140 GeV/c)	2.193×10^6	339874
Dijet	J4(140 GeV/c < p_T < 280 GeV/c)	8.784×10^4	366164
Dijet	J5(280 GeV/c < p_T < 560 GeV/c)	2.328×10^3	361174
Dijet	J6(560 GeV/c < p_T < 1120 GeV/c)	33.846	365709

7.2.1 Background Rejection

In order to reduce the background we involved the same observables as used in the black hole analysis. Figure 7.3 shows the $\sum |p_T|$ of all observable objects in an event. The background drops rapidly with increasing $\sum |p_T|$, while the signal is slowly increasing before dropping. At $\sim 2\text{TeV}/c$ the signal exceeds the background. While Figure 7.4 shows the number of objects that passes the selection criteria from Table 7.1. At N > 14, the signal exceeds the background. Another quantity used for separating signal from background is the number of high-p_T objects. Figures 7.5 and 7.6 show the p_T distributions for the 4th and 5th highest p_T objects. Again a clear separation is found between the signal and background. In Figure 7.5 the signal becomes larger than the background at $p_T \geq 250$ GeV/c and for Figure 7.6 we find that the signal becomes larger than the background at $p_T \geq 160$ GeV/c.
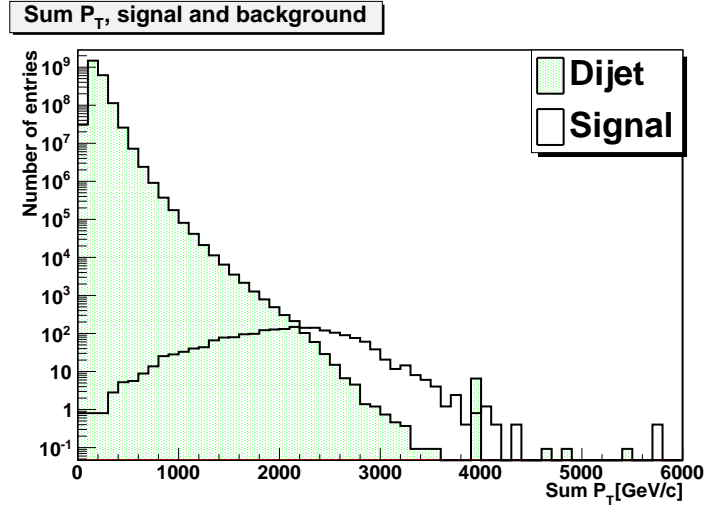
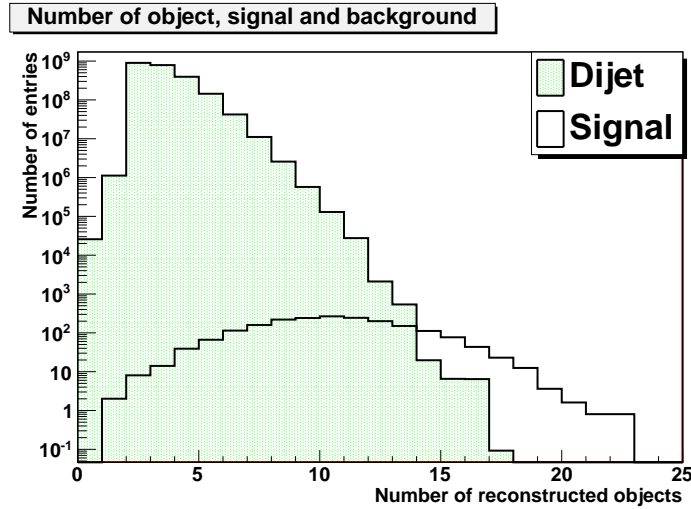*Figure 7.3:* The $\sum |p_T|$ distributions for signal and background.

Figure 7.4: The number of reconstructed objects for signal and background.

Optimization

The observables in Figures 7.3-7.6 can all be used to optimize the signal yield. We follow the same procedure that was used in the black hole analysis (see section 6.2.3), for the $\sum |p_T|$ and p_T of the 5th leading object. Figure 7.7 shows the significance as a function of the minimum requirement on $\sum |p_T|$. The highest significance is achieved for $\sum |p_T| \geq$ 2 TeV/c. This is the value where signal and background are equal (see Figure 7.3). The optimization for p_T for the 5th leading object is shown in Figure 7.8. The best significance
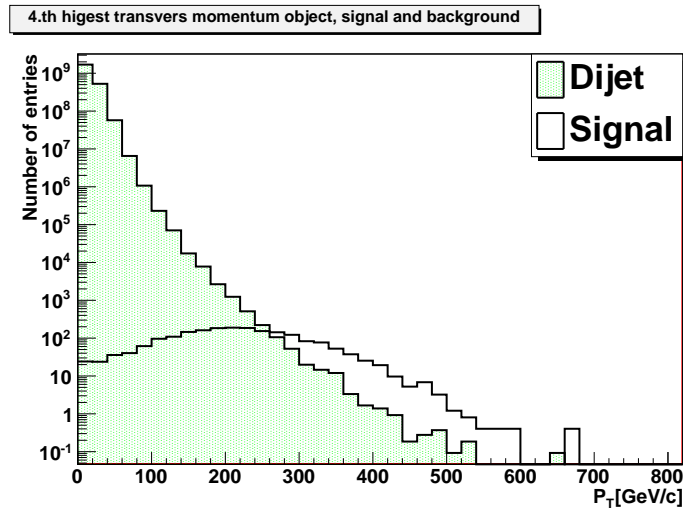
Figure 7.5: Transverse momentum of the 4th leading object.
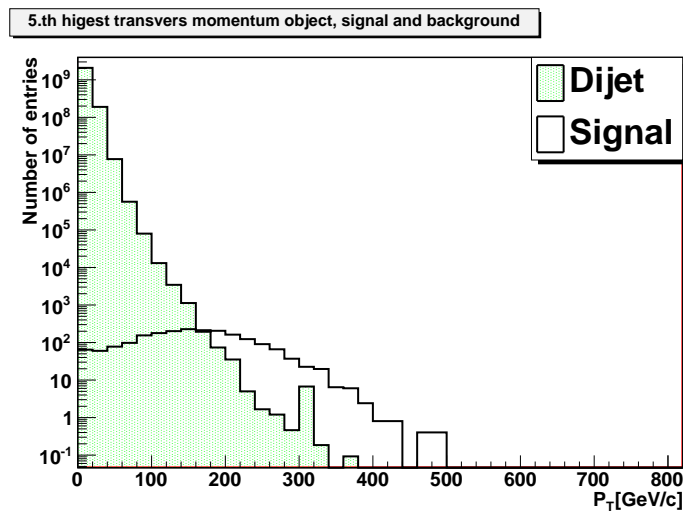

Figure 7.6: Transverse momentum of the 5th leading object.

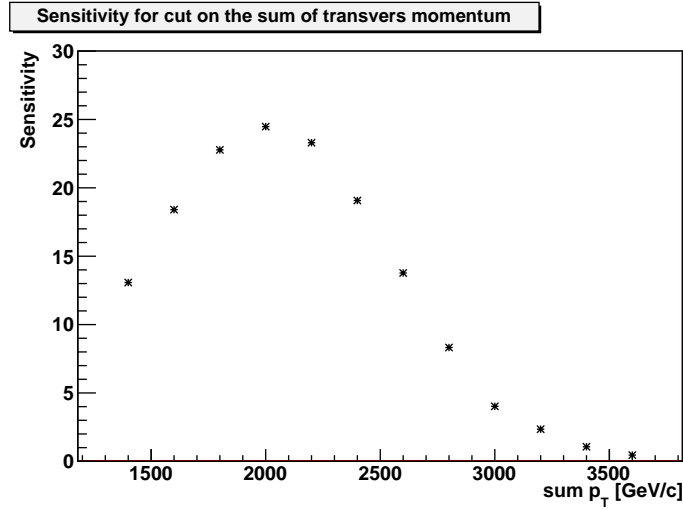is achieved for $p_T \geq 160$ GeV/c. Here again the signal and background is equal (see Figure 7.6).

Figure 7.7: Significance R $= (S/\sqrt{S+B})$ as a function of $\sum|p_T| > \sum|p_T|_{min}$.
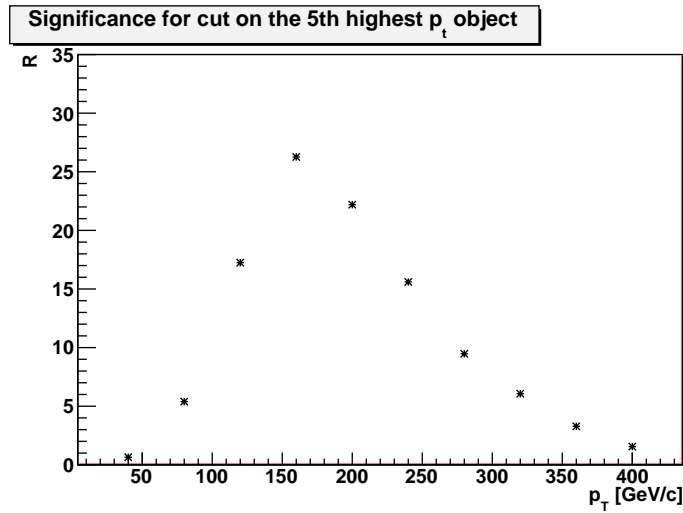

Figure 7.8: Significance R $= (S/\sqrt{S+B})$ as a function of $p_T > p_{T_{min}}$ for p_T the 5th leading object.

We plotted the $\sum |p_T|$ and the p_T of the 5th leading object vs the mass, for the string ball signal and the J5 dijet background. Figure 7.9 show the $\sum |p_T|$ plotted against the mass. The horizontal line indicate the optimal selection requirement. Figure 7.10 shows the p_T
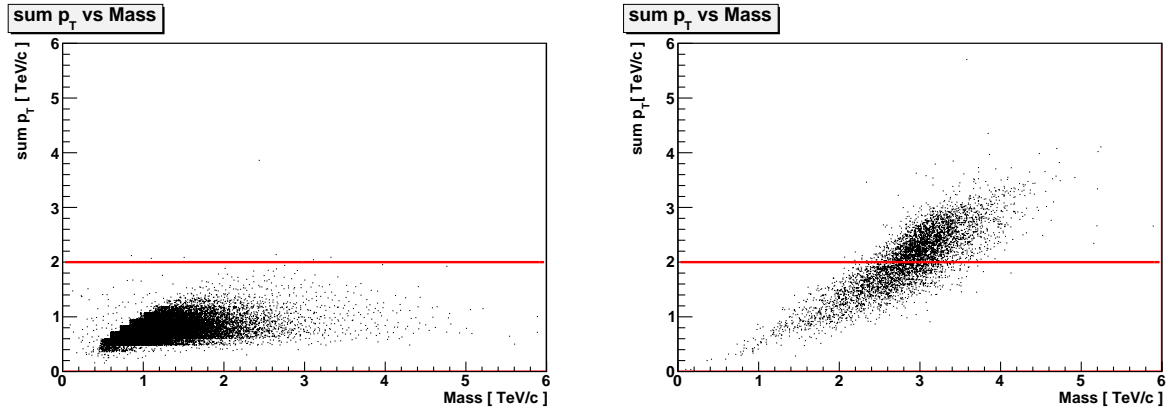

Figure 7.9: (*Left:*) $\sum |p_T|$ vs string ball invariant mass for J5 background. (*Right:*) $\sum |p_T|$ vs string ball invariant mass for the string ball sample.

of the 5th leading object, plotted against the mass for the J5 background and the signal. The horizontal line indicate the optimal cut value. Not manny J5 background event is above the horizontal lien.
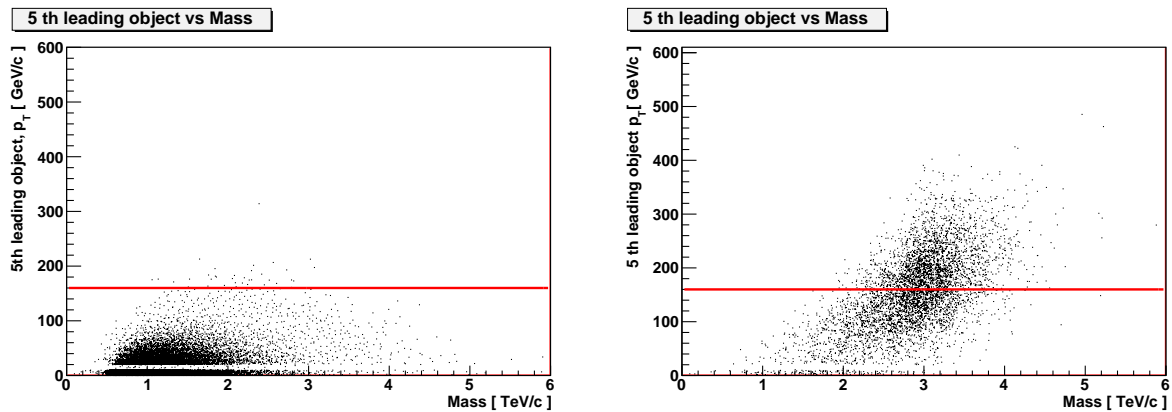

Figure 7.10: (*Left:*) p_T for the 5th leading object vs the invariant mass for the J5 background. (*Right:*) p_T for the 5th leading object vs the invariant mass for the string ball signal.

Invariant Mass Reconstruction after optimization

The final selection for the reconstruction of string balls with a mass of 3 TeV/c^2, is done by requiring that $\sum |p_T| > 2$ TeV/c, p$_T > 160$ GeV/c for the 5th leading object and at least 5 object passes selection requirement from Table 7.1. Figure 7.11 shows the invariant mass distribution, with and without log scale. As shown, the signal is about 2 orders of magnitude larger than the background. Table 7.3 shows the different selection efficiencies, and the number of signal and background events that pass the different selection criteria for 1 fb^{-1} of data. See Appendix A, for more info on the different selection criteria.
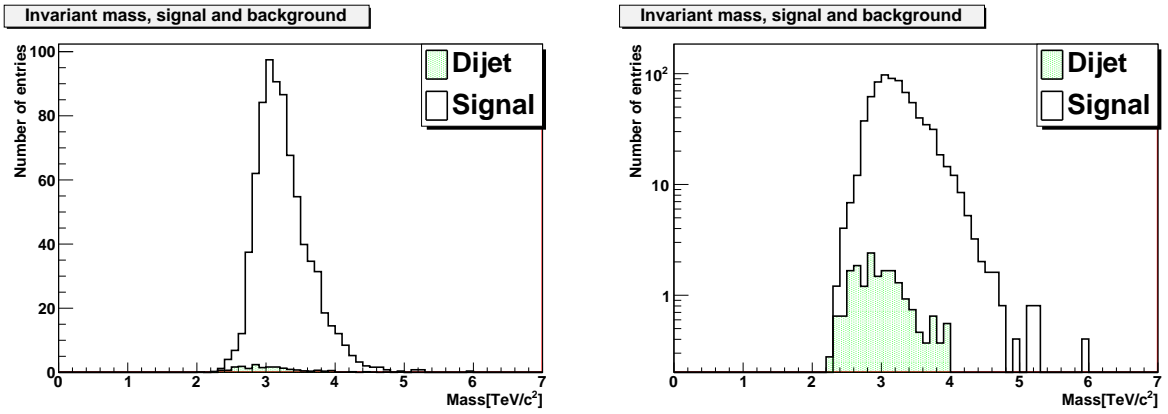

Figure 7.11: (*Left:*)the invariant mass distribution. (*Right:*) the invariant mass distribution with log scale.

Table 7.3: String ball selection efficiencies, the event number is rounded of to the closes integer number. The background uncertainties are rounded up to closes integer number.

String ball reconstruction efficiency			
Cut value	Efficiency	Signal events	Background events
$\sum p_T > 2.0$ TeV	56.2 %	1124	718 ± 17
Leading 5.th order: p$_T > 160$ GeV	46.9 %	938	318 ± 55
Combined cut	39.1 %	782	20 ± 4

To find the discovery potential for string balls in ATLAS, we calculated the significance as a function of luminosity, see Equation 6.3. We require that $\sum |p_T| > 2$ TeV/c, and $p_T > 160$ GeV/c for the 5th leading object. Figure 7.12 shows the significance as it variates with luminosity. We find that for string balls signal with a cross section of 2 pb and mass of 3 TeV/c^2, the significance gives 5σ value, for an luminosity of 35 pb^{-1}.
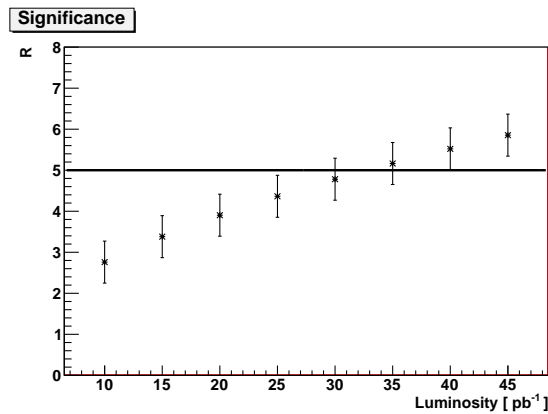

Figure 7.12: Significance for string ball discovery as a function of luminosity

If string balls are not found in first period of data taking with ATLAS, limits on the cross section can be set. We plotted the significance, Equation 6.3, as a function of the signal cross section. Figure 7.13 shows the significance as a function of signal cross section, when require that $\sum |p_T| > 2$ TeV/c, and $p_T > 160$ GeV/c for the 5th leading object. If the signal cross section is larger then 0.1 pb, a 5σ discovery is possible. If no sting ball events
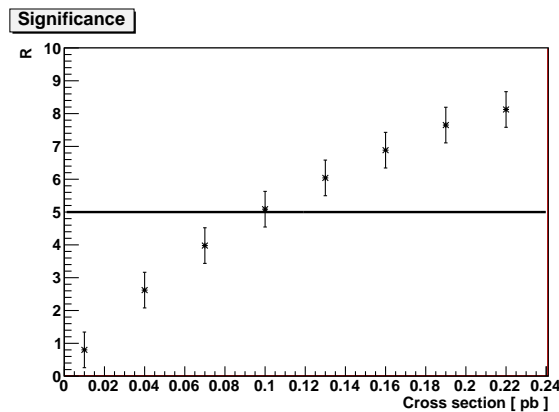

Figure 7.13: Significance as a function of cross section.

are discovered in the first 1 fb^{-1} of data, limits could be set on the cross section. Using the

Bayesian approach for the case if we have no observed events after 1 fb^{-1}, and assuming our reconstruction efficiency. The 90% upper limit is then set by

$$\frac{\nu_{up}}{\epsilon \cdot \mathscr{L}} = \frac{2.30}{0.391 \cdot 1 fb^{-1}} = 5.88 fb. \tag{7.1}$$

If no observed sting balls are found in the first 1 fb^{-1} of data, 90% upper limit (95%) can be set at $\sigma_{BH} < 5.88$ fb (7.67 fb).

Chapter 8

Conclusion

In this thesis we have reconstructed black hole and string balls from Monte Carlo simulated data. We have been studying ways to remove standard model background, from the signal. Black holes and string balls will have a quite remarkable characteristic feature compared to standard model processes. This allows for a good separation between signal and background.

For the black hole study, we derived a reconstruction requirement that relay on a minimum of five reconstructed object, $\sum |p_T| > 2.8$ TeV/c and the transverse momentum for the 5th leading object is $p_T > 200$ GeV/c. At a center of mass energy of 10 TeV, ATLAS has a great discovery potential for black holes.

We have also studied string ball production and decay, which are more likely to be produced at lower energy collisions. We have developed selection criteria for reconstruction of string balls, which relay on $\sum |p_T| > 2$ TeV/c, and $p_T > 160$ GeV/c for the 5th leading object. ATLAS will have a great possibility of discovering string balls, already in the first period of data taking.

Future steps in this analysis will be to start looking at real data. Where we will start to search for black holes and string balls. If not found, limits can be set on their production cross section.

Appendix A

A.1 String ball mass reconstruction

In Chapter 7 we reconstructed the invariant mass for string balls, after requirng $\sum |p_T| > 2$ TeV and $p_T > 160$ GeV for the 5th leading object. In this chapter the individual distributions are shown. All plots in this chapter are normalized to an integrated luminosity of 1 fb^{-1}.

Figure A.1 shows the invariant mass distribution after requiring $\sum |p_T| > 2$ TeV, while Figure A.2 shows the invariant mass distribution after the require the 5th leading object to have $p_T > 160$ GeV. The significance can also be calculated as a function, when one of the
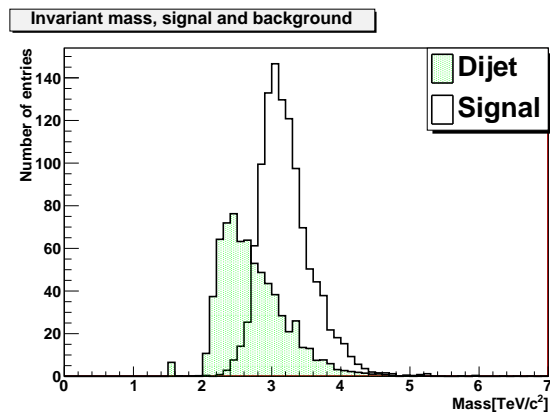

Figure A.1: Invariant mass distribution with requirement that $\sum |p_T| > 2$ TeV/c.

selection requirement have a constant value, and the the other changes in steps. Figure A.3 shows the significance when $\sum |p_T|$ is constant, and when the p_T for the 5 leading objet is constant.
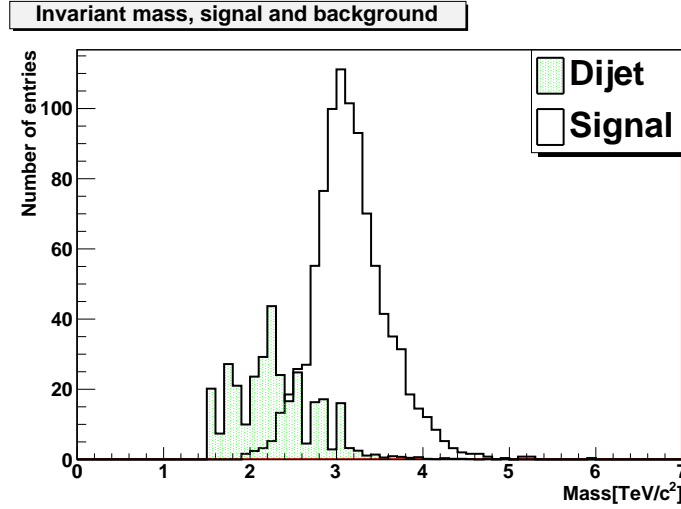
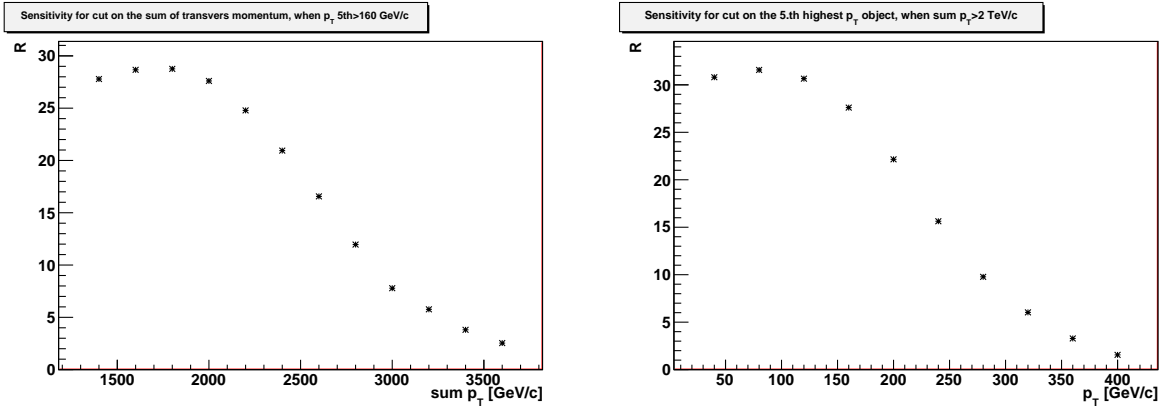*Figure A.2:* Invariant mass distribution with requirement that $p_T > 160$ GeV for the 5th leading object.

Figure A.3: (*Left*) Shows the significance ($S/\sqrt{S+B}$) when the p_T for the 5th leading object is greater then 160 GeV/c as a function of $\sum |p_T| > \sum |p_T|_{min}$. (*Right*) Shows the significance when $\sum |p_T| > 2$ TeV/c and the p_T for the 5th leading object is $p_T > p_{T_{min}}$.

We also attempted to optimize the signal and background yield using the momentum of the 4th leading object. This was found not to give as nice result as for the 5th leading object. Figure A.4 shows the optimum value for a p_T cut on the 4th leading object. It gives the highest significance for $p_T \geq 240$ GeV/c. In Figure A.5 we used this value to reconstruct the invariant mass of the string ball. Table A.1 shows the number of events that pass the selection criteria for the signal and background.
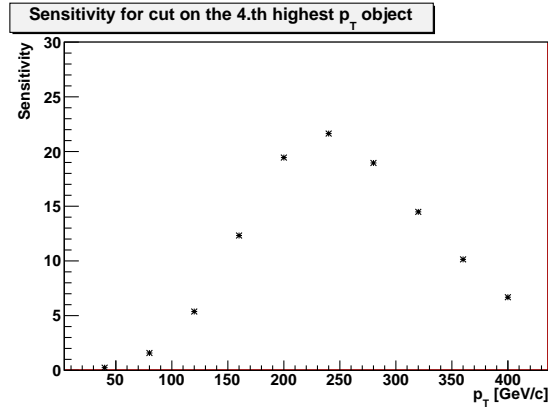
Figure A.4: Significance $(S/\sqrt{S+B})$ as a function of $p_T > p_{T_{min}}$ for p_T the 4th leading object.
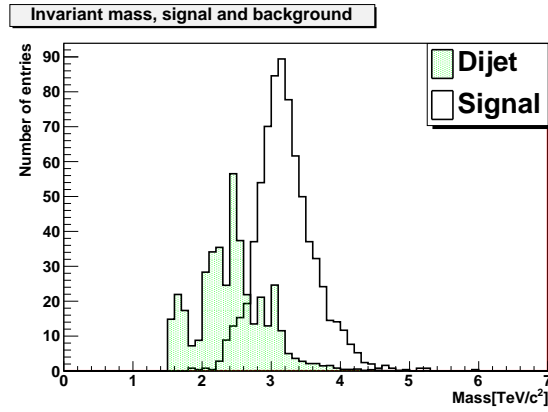

Figure A.5: Invariant mass distribution with requirement that $p_T > 240$ GeV for the 4th leading object.

Table A.1: String ball selection efficiencies with 4th leading object.

String ball reconstruction efficiency			
Cut value	Efficiency	Signal events	Background events
$p_T > 240$ GeV/c	37.2 %	743	414

73

A.2 Leading object

We have optimized our signal selection using the 4th and 5th leading object. We find that the optimization using the 1th, 2th and 3th leading object are not good observables to separate the signal and background. Figure A.6 shows the p_T for the 1th, 2th and 3th leading object for the string ball study. The distributions are normalized to 1 fb^{-1} of data. The background dominates in all these distributions (which also is the case in the black hole study).
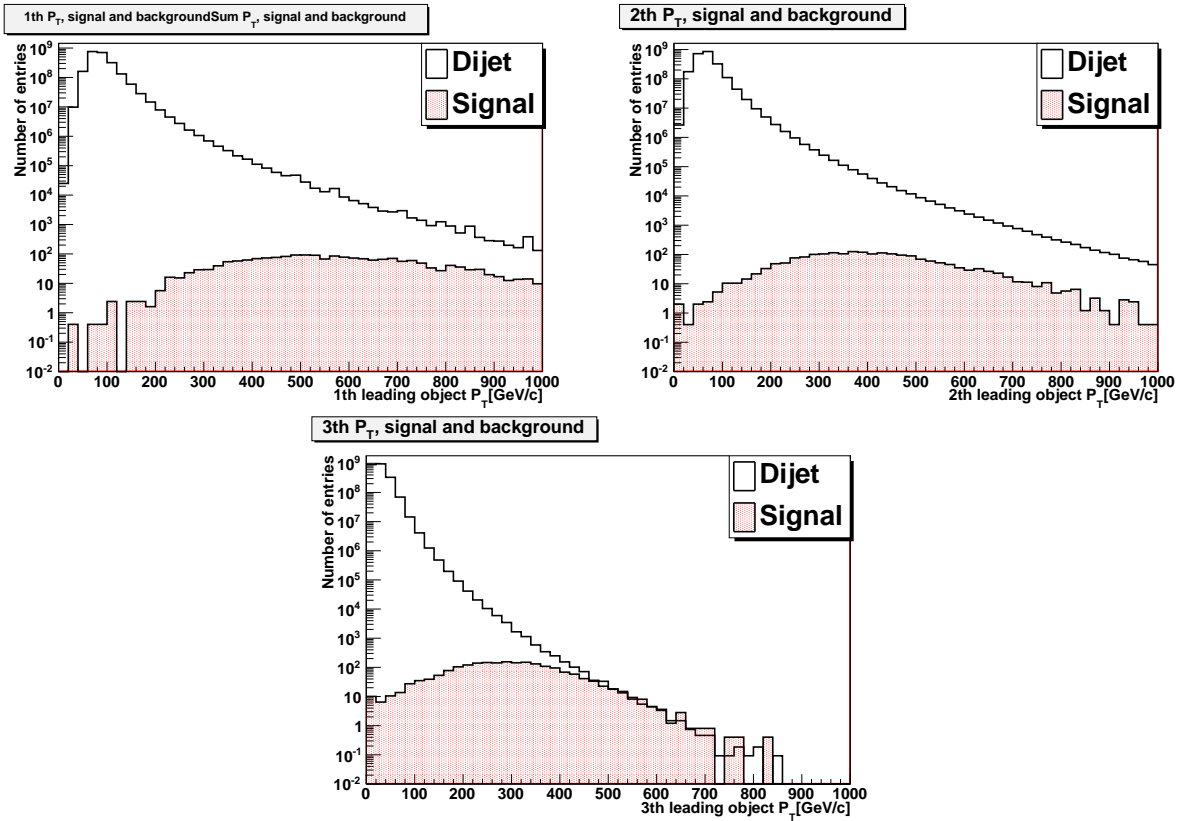

Figure A.6: (*Upper left:*) transverse momentum of the leading object. (*Upper right:*) transverse momentum of the 2th leading object. (*Lower center:*) transverse momentum of the 3th leading object.

Bibliography

[1] http://atlas.ch/photos/events-simulated-black-hole.html.

[2] http://pdg.lbl.gov/2009/listings/rpp2009-list-neutrino-prop.pdf.

[3] C. Amsler et al. (Particle Data Group). The review of particle physics. *Physics Letters B667, 1*, 2008.

[4] Gell-Mann Murray. The interpretation of the new particles as displaced charged multiplets. *Il Nuovo Cimento 4: 848.*, 1956.

[5] Roger J.N. Phillips Vernon D. Brager. *Collider Physics-Updated Edition.* Westview Press, 1996.

[6] N. Arkani-Hamed, S. Dimopoulos, and G. R Dvali. The hierarchy problem and new dimensions at a millimeter. *Phys. Lett.*, B429:263–272, 1998. hep-ph/9803315.

[7] CDF Collaboration: T. Aaltonen et al. Search for large extra dimensions in the production of jets and missing transverse energy in $p\bar{p}$ collisions at $\sqrt{s} = 1.96$ tev. *Phys.Rev.Lett.101:181602*, 2008. arXiv:hep-ex/0605101v1.

[8] L. Randall and R. Sundrum. A large mass hierarchy from a small extra dimension. *Phys. Rev. Lett*, 83:3370, 1999. hep-ph/9905221.

[9] V. M. Abazov et al. [D0 Collaboration]. Search for randall-sundrum gravitons in dilepton and diphoton final states. *Phys. Rev. Lett.*, 95(9):091801, Aug 2005.

[10] G. Landsberg [D0 and CDF Collaboration]. Collider searches for extra dimensions. hep-ex/0412028.

[11] Myers R C and Perry M J. *ann.. Phys. (N.Y.)*, 172:304, 1986.

[12] Douglas M. Gingrich and Kevin Martell. Study of highly excited string at the large hadron collider. *Phys. Rev. D.*, 78.115009, 2008.

[13] Savas Dimopoulos and Greg Landsberg. Black holes at the large hadron collider. *Physical Review Letters*, 87, 2001.

[14] Hawking S W. *Commun. Math. Phys.*, 43, 1975.

[15] Greg Landsberg. Black holes at future colliders and beyond. *J.Phys*, G32:R337–R365, 2006. hep-ph/0607297v1.

[16] Steven B. Giddings. Black hole production in tev-scale gravity, and the future of high energy physics. hep-ph/0110127v3.

[17] Douglas M. Gingrich. Missing energy in black hole production and decay at the large hadron collider, 2007. arXiv:0706.0623v2.

[18] D. Amatia and J.G. Russo. Fundamental strings as black bodies. 1999. hep-th/9901092v2.

[19] Savas Dimopoulos and Roberto Emparan. String balls at the lhc and beyond. 2001. hep-ph/0108060v1.

[20] ATLAS Collaboration. G WEIGLEIN et al. Physics interplay of the lhc and the ilc. *Physics Reports Volume 426 Issues 2-6*, April 2006. hep-ph/0410364.

[21] Communication Group. Cern faq, lhc the guide, February 2009. CERN-Brochure-2009-003-Eng.

[22] ATLAS Collaboration. The atlas experiment at the cern large hadron collider, 2008.

[23] https://twiki.cern.ch/twiki/pub/Atlas/MuonPerformancePublicPlots/DimuonMassOppSignApril2010.eps.

[24] A brief introduction to pythia 8.1. http://home.thep.lu.se/ torbjorn/pythia8/pythia8100.pdf.

[25] G. Corcella et al. Herwig 6.5. *JHEP 0101 010*, 2001. hep-ph/0210213.

[26] http://projects.hepforge.org/sherpa/dokuwiki/doku.php.

[27] http://borut.home.cern.ch/borut/.

[28] M.L. Mangano et al. Alpgen, a generator for hard multiparton processes in hadronic collisions. *JHEP 0307:001*, 2003. hep-ph/0206293.

[29] Johan Alwall et al. Madgraph/madevent v4: The new web generation. *JHEP0709:028*, 2007. arXiv:0706.2334v1 [hep-ph].

[30] S. Frixione and B.R. Webber. Matching nlo qcd computations and parton shower simulations. *JHEP 0206 029*, 2002. hep-ph/0204244.

[31] http://geant4.cern.ch/.

[32] http://www.hep.ucl.ac.uk/atlas/atlfast/.

[33] https://twiki.cern.ch/twiki/bin/view/Atlas/WorkBookFullChain.

[34] P. Richardson C.M. Harris and B.R. Webber. Charybdis: A black hole event generator. *JHEP 0308:033*, 2003. hep-ph/0307305.

[35] P. Kanti C.M. Harris. Hawking radiation from a (4+n)-dimensional black hole: Exact results for the schwarzschild phase. *JHEP 0310:014*, 2003. hep-ph/0309054.

[36] De-Chang Dai, Glenn Starkman, Dejan Stojkovic, Cigdem Issever, Eram Rizvi, and Jeff Tseng. Blackmax: A black-hole event generator with rotation, recoil, split branes, and brane tension. *Phys. Rev. D*, 77(7):076007, Apr 2008.

[37] G. Duckeck et al. Atlas computing technical design report. *tech. rep., CERN*, 2005. http://doc.cern.ch//archive/electronic/cern/preprints/lhcc/public/lhcc-2005-022.pdf.

[38] https://twiki.cern.ch/twiki/bin/view/Atlas/WorkBookAthenaFramework.

[39] ATLAS Collaboration. Expected performance of the atlas experiment, detector, trigger and physics, Desember 2008.

[40] The ATLAS Collaboration. Search for highly-excited string states with atlas. *ATL-PHYS-PUB-2009-011*.

[41] https://twiki.cern.ch/twiki/bin/view/AtlasProtected/TSGMC7TeV.